PROCEEDINGS A

royalsocietypublishing.org/journal/rspa

Research

Cite this article: Brennan M, Yeo EF, Pearce P, Dalwadi MP. 2026 Effective permeability conditions for diffusive transport through impermeable membranes with gaps. *Proc. R. Soc. A* **482**: 20250703.
https://doi.org/10.1098/rspa.2025.0703

Received: 18 August 2025
Accepted: 24 November 2025

Subject Areas:
applied mathematics, mathematical modelling, biophysics

Keywords:
membrane conditions, homogenized boundary conditions, method of multiple scales, periodic interface, homogenized coupling conditions, effective conditions

Author for correspondence:
Mohit P. Dalwadi
e-mail: mohit.dalwadi@maths.ox.ac.uk

Electronic supplementary material is available online at https://doi.org/10.6084/m9.figshare.c.8217042.

THE ROYAL SOCIETY PUBLISHING

Effective permeability conditions for diffusive transport through impermeable membranes with gaps

Molly Brennan[1], Edwina F. Yeo[1], Philip Pearce[1] and Mohit P. Dalwadi[1,2]

[1]Department of Mathematics, University College London, London WC1E 6BT, UK
[2]Mathematical Institute, University of Oxford, Oxford OX2 6GG, UK

MB, 0009-0002-6469-0832; EFY, 0000-0003-2635-4985; PP, 0000-0001-5788-3826; MPD, 0000-0001-5017-2116

Membranes regulate transport in a wide variety of industrial and biological applications. The microscale geometry of the membrane can significantly affect overall transport through the membrane, but the precise nature of this multiscale coupling is not well characterized in general. Motivated by the application of transport across a bacterial membrane, we use formal multiscale analysis to derive explicit effective coupling conditions for macroscale transport across a two-dimensional (2D) impermeable membrane with periodically spaced gaps, and validate these with numerical simulations. We derive analytic expressions for macroscale membrane quantities, such as the effective permeability, in terms of the microscale geometry. Our results generalize the classic constitutive membrane coupling conditions to a wider range of membrane geometries and time-varying scenarios, e.g. we demonstrate that the unsteady conditions can gain a memory property and depend on the system history. By applying our effective conditions to small-molecule transport through gaps in bacterial membranes called porins, we predict that membrane permeability here is primarily dominated by membrane thickness. Furthermore, we predict how alterations to membrane microstructure, e.g. via

changes to porin expression, might affect overall transport. These results apply to other physical applications with similar membrane structures, from medical and industrial filtration to carbon capture.

royalsocietypublishing.org/journal/rspa Proc. R. Soc. A 482: 20250703

1. Introduction

Membrane transport plays an important role in many biological and industrial settings, including haemodialysis for virus filtration in laboratories [1], kidney dialysis to treat renal failure [2], carbon capture from flue gas [3], wastewater treatment [4] and bacterial communication [5]. In many of these applications, transport across membrane structures, such as channels in the membrane, occurs over much smaller lengthscales than the overall system scales. Membrane-mediated transport is therefore inherently multiscale, creating difficulties in resolving disparate lengthscales in mathematical modelling. A common way to deal with these difficulties is to use constitutive macroscale relationships motivated by physical intuition. These relationships typically link the flux through the membrane to the concentration difference across it, with standard conditions of the form

$$\frac{\partial c}{\partial n}|_{\text{above}} = \frac{\partial c}{\partial n}|_{\text{below}} = P_{\text{eff}}(c_{\text{above}} - c_{\text{below}}), \tag{1.1}$$

where c is the solute concentration, $\partial/\partial n$ is the derivative normal to the membrane and P_{eff} is a (typically fitted) constant of proportionality [6–10]. Other authors have also incorporated the effect of membrane transport by coupling production and decay of concentrations on either side of the membrane [11,12]. While these constitutive conditions are generally successful in replicating observed phenomena in the parameter regimes in which their coefficients are estimated, and deal with the issue of computational complexity induced by disparate lengthscales, they may not be able to predict transport in new regimes because the lumped parameters within constitutive relations do not explicitly depend on microscale geometry.

To address the multiscale challenge of accounting for microscale channel effects in larger scale models, many authors have sought to derive effective conditions representing transport across membranes. A review of early work in this field is presented in [13]. Several authors consider homogenization of a surface of periodically varying boundary conditions in order to describe effective membrane behaviour for various transport mechanisms, for example using (periodic) patches of perfect absorbers on an otherwise reflecting surface [14–18]. With this method, one can derive effective boundary conditions for the bulk concentration in the region above, providing an effective uptake equation on one side of a membrane surface.

Transport across thin membranes has been studied in [19,20], where the authors consider advective transport (including diffusive transport and surface reactions in the latter paper), deriving appropriate effective jump conditions on the stress and solute flux across a membrane. In the absence of any surface reactions, the authors calculate that the leading-order concentration and concentration flux are continuous across the effective membrane surface to leading order. This is in part owing to the thin membrane geometry that the authors investigate, which cannot sustain a leading-order concentration jump across the membrane. Here, we are interested in a different class of membranes, those across which significant concentration differences can be sustained by membrane geometry alone. As such, we include a physical membrane with a significant thickness as part of our model as well as domains both above and below the membrane, in contrast to the thin membrane or single domain problems discussed above. Several authors have considered similar problems of membrane transport from a rigorous standpoint, proving convergence of specific effective problems and solution forms [21–24]. These typically take the form of a derived microscale system to be solved, coupled to a macroscale problem, and provide mathematical insight into the structure of membrane transport problems. However, owing to their generality,

one typically cannot solve explicitly the microscale systems derived therein. Here, in order to gain further insight into the coupling between microscale geometry and macroscale function, we investigate a specific microscale geometry in which we can derive explicit relationships between scales.

We are primarily motivated by applications involving bacterial membranes—more specifically, the outer membrane of Gram-negative bacteria—where transport is typically limited to specific channels with binding sites or non-specific channels, called porins, which provide a size-restricted passageway for small water-soluble molecules [8]. Understanding transport across bacterial membranes is vital because the ability of bacterial populations to regulate complex collective behaviours that facilitate infection and resistance relies on the exchange and build up of small diffusible signal molecules that cross bacterial membranes [25,26]. The disruption of communication pathways is therefore a proposed target for interventions in preventing bacterial infection, particularly owing to the growing numbers of antibiotic resistant bacteria [27]. Transport is also fundamental in current prevention methods of bacterial infection, such as in antibiotic delivery, in which porins play a key role [28]. For many species of bacteria, antibiotics must cross bacterial membranes in order to be effective. In particular, transport across the outer membrane of Gram-negative bacteria is complicated by many factors. For example, antibiotic molecules are often of a similar size to the porins and channels in the membrane, so steric effects, including interaction with channel surfaces, can be a limiting factor in antibiotic permeation [28]. In addition, interactions between antibiotic molecules and binding sites in specific channels and the charge of the molecules can enhance transport [8]. However, for transport of both signal and antibiotic molecules in bacterial populations, processes that occur on the scale of membrane channels can generate effects that occur over the colony scale, again highlighting the need for multiscale insight. Here we wish to specifically understand how membrane microstructure itself affects bacterial scale transport, independent of channel interactions and finite-size particle effects, focusing on diffusion of small solutes (typically with a molecular mass cut-off of around 600 Da) through general porins facilitating non-specific diffusion [28].

In this paper, we use homogenization via the method of multiple scales to derive explicit coupling conditions across an impermeable perforated membrane, allowing us to connect the concentration fields away from the membrane. Our membrane consists of an impermeable barrier periodically punctured with channels that are thin compared to their spacing. We consider both the limits in which gap height is much larger than gap width, which we call the long thin channel limit, and the limit in which gap height is around the same size as gap width, which we refer to as the $\mathcal{O}(1)$ aspect ratio limit. The multiscale (asymptotic) techniques we use to derive the effective coupling conditions to apply across our membrane are similar to those used to derive effective coupling conditions in wave transmission problems in Faraday cages in [29,30]. More generally, boundary homogenization methods are widely used to obtain coupling conditions for wave transmission problems across thin interfaces [31–33]. We exploit the extreme disparity in the spatial scales in our problem, with our derived effective coupling conditions formally incorporating channel lengthscale effects over bacterial lengthscales. Our results allow one to formally treat the membrane as a continuous boundary with effective conditions which couple the concentration on either side, and allow us to understand how these effective conditions depend on the microscale properties of the membrane. We derive coupling conditions for both steady and unsteady transport across the membrane. Notably, the coupling conditions we derive for the steady problem are mathematically equivalent to the standard permeability equation (1.1), and we are able to explicitly determine the effective permeability P_{eff} in terms of the microscale membrane geometry. In the unsteady case, we derive new effective coupling conditions which gain terms with integrals in time, i.e. generating emergent memory properties. We use our results to investigate how the microscale structure of the membrane affects its effective permeability. Our analysis allows us to understand in which limits the constitutive models are valid, when one might expect them to break down, and the appropriate form of the coupling conditions in these scenarios.

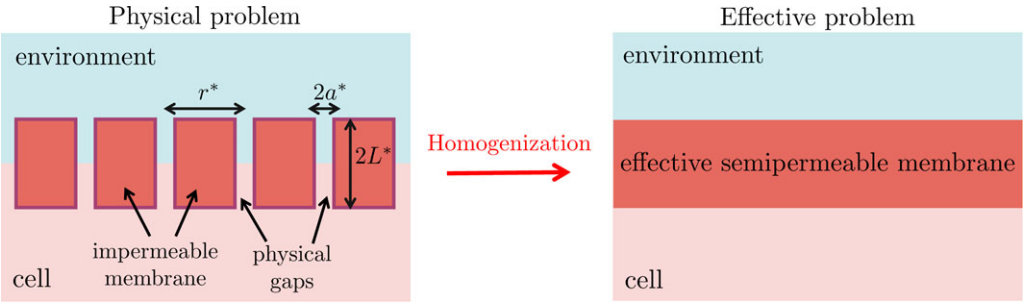

Figure 1. Schematic demonstrating the output of our homogenization procedure. We systematically derive effective coupling conditions that allow us to accurately model the membrane as a continuous and homogeneous boundary, removing the need to account for each gap individually. Dimensional parameters are defined in §2.

The structure of this paper is as follows. In §2, we introduce the mathematical description of our problem, and discuss the asymptotic structure and specific asymptotic regions of the problem. In §3, we consider the steady problem and, using boundary layer theory and homogenization via the method of multiple scales, we systematically derive the appropriate effective coupling conditions. For clarity of presentation we show the analysis of the long thin channel limit in the main text, and present analysis of the $\mathcal{O}(1)$ aspect ratio limit in appendix A. In §4, we consider the unsteady problem, allowing us to determine when it is appropriate to use the steady effective conditions we derive in §3, and the appropriate unsteady conditions to use when it is not. We also present an early-time approximation to our effective coupling conditions, when they are generically slow to converge, using an asymptotic Euler–Maclaurin summation. In §5, we validate our effective results against simulations of the full membrane geometry. In §6, we explore the implications of our results and compare them to other models for membrane and channel transport. Finally, in §7, we discuss our results and highlight how they could be used in other applications.

2. Mathematical framework

We consider the diffusive transport of a solute, representing, e.g. autoinducers or antibiotics, in the two-dimensional (2D) domain $\Omega^* = \{(x^*, y^*) \in \mathbb{R}^2\}$ with the membrane modelled as an impermeable wall with finite thickness, $2L^*$, periodically perforated with physical gaps of width $2a^*$ each separated by a distance of r^*. These gaps model non-specific channels, i.e. channels with no interaction or binding, across which a solute consisting of small molecules diffuses freely. Mathematically, we describe the impermeable part of the membrane (i.e. the membrane excluding the gaps) as $\Gamma^* = \{\boldsymbol{x}^* = (x^*, y^*) : x^* \in \mathbb{R}, y^* \in (-L^*, L^*)\} \backslash \{\boldsymbol{x}^* = (x^*, y^*) : x^* \in (r^* j - a^*, r^* j + a^*), y^* \in (-L^*, L^*), j \in \mathbb{Z}\}$ with $\partial\Gamma^*$ denoting its boundary. We denote our solute concentration by $c^*(\boldsymbol{x}^*, t^*)$, where $\boldsymbol{x}^*$ is the spatial vector coordinate and t^* is time. We use homogenization via the method of multiple scales to derive effective coupling conditions across the membrane (illustrated schematically in figure 1). The problem we consider can be thought of as the 'inner' problem (in the language of matched asymptotic expansions) in which we derive the correct coupling conditions for an unsteady 'outer' problem which sees the membrane as a curved interface. As such, we consider a locally flat membrane for the inner problem, noting that our results will be valid for membranes with moderate curvature in the outer problem.

We consider diffusive transport through the impermeable membrane. Mathematically, this is given by

$$\frac{\partial c^*}{\partial t^*} = D^* \nabla^{*2} c^*, \quad \boldsymbol{x}^* \in \Omega^* \backslash \Gamma^*, \tag{2.1a}$$

Table 1. Dimensional membrane parameters for a range of bacterial species.

dimensional parameter	physical interpretation	size (nm)	ref.
R^*	macroscale length (e.g. cell radius)	360–3000	[34,35]
a^*	porin radius (half porin width)	0.325–4	[8,36]
$2L^*$	porin length (membrane thickness)	2.4–12	[37–39]
r^*	centre-to-centre porin spacing	9–10.8	[36,40]

$$\frac{\partial c^*}{\partial n} = 0, \quad \boldsymbol{x}^* \in \partial \Gamma^* \tag{2.1b}$$

and

$$c^*(\boldsymbol{x}^*, 0) = c^*_{\text{init}}(\boldsymbol{x}^*), \quad \boldsymbol{x}^* \in \Omega^* \backslash \Gamma^*, \tag{2.1c}$$

where c^*_{init} denotes a general initial condition, D^* is the constant diffusivity of the solute and $\partial/\partial n$ denotes the derivative in the direction of the outward pointing normal to the membrane. As we assume no solute is absorbed on the impermeable membrane walls, equation (2.1*b*) describes no flux boundary conditions. While far-field conditions ($y^* \to \pm\infty$) are also required to fully close the problem, our analysis is agnostic to their specific form for non-pathological cases and so we do not prescribe these for generality. Our overarching goal is to derive the effective coupling conditions that link the 'internal' concentration as $y^* \to -\infty$, below the membrane, to the 'external' concentration at $y^* \to \infty$ above the membrane.

We list typical parameter values for bacterial systems, which motivate our specific geometry, in table 1. In general, bacteria can regulate the expression of porins, for example, lowering expression in response to environmental factors to reduce permeability to, e.g. antibiotics. They can also alter porin configuration, changing them to a closed configuration in response to voltage, acidic pH and binding of certain molecules [36,41]. However, for simplicity, here we consider purely static membrane geometries neglecting temporal effects in porin expression.

We non-dimensionalize the problem using the following macroscale scalings:

$$t^* = \frac{R^{*2}}{D} t, \quad \boldsymbol{x}^* = R^* \boldsymbol{x}, \quad c^* = c_0^* c \quad \text{and} \quad c^*_{\text{init}} = c_0^* c_{\text{init}}, \tag{2.2}$$

where R^* is a characteristic macroscale length (e.g. cell radius) and c_0^* is a characteristic macroscale concentration. Applying our non-dimensionalization equation (2.2), to our governing equations (2.1), we have

$$\frac{\partial c}{\partial t} = \nabla^2 c, \quad \boldsymbol{x} \in \Omega \backslash \Gamma, \tag{2.3a}$$

$$\frac{\partial c}{\partial n} = 0, \quad \boldsymbol{x} \in \partial \Gamma \tag{2.3b}$$

and

$$c(\boldsymbol{x}, 0) = c_{\text{init}}(\boldsymbol{x}), \quad \boldsymbol{x} \in \Omega \backslash \Gamma. \tag{2.3c}$$

Our dimensionless membrane is now defined as

$$\begin{aligned} \Gamma = \{\boldsymbol{x} = (x, y) : x \in \mathbb{R}, y \in (-L, L)\} \backslash \\ \{\boldsymbol{x} = (x, y) : x \in (\delta j - \delta\varepsilon, \delta j + \delta\varepsilon), y \in (-L, L), j \in \mathbb{Z}\}, \end{aligned} \tag{2.4}$$

where we have introduced the rescaled parameters

$$\delta = \frac{r^*}{R^*}, \quad \varepsilon = \frac{a^*}{r^*} \quad \text{and} \quad L = \frac{L^*}{R^*}. \tag{2.5}$$

These parameters δ, $\delta\varepsilon$ and L now represent the non-dimensional channel spacing, channel width and membrane thickness, respectively. We illustrate our full non-dimensional geometry with the membrane and porins alongside the asymptotic structure of our problem in figure 2.

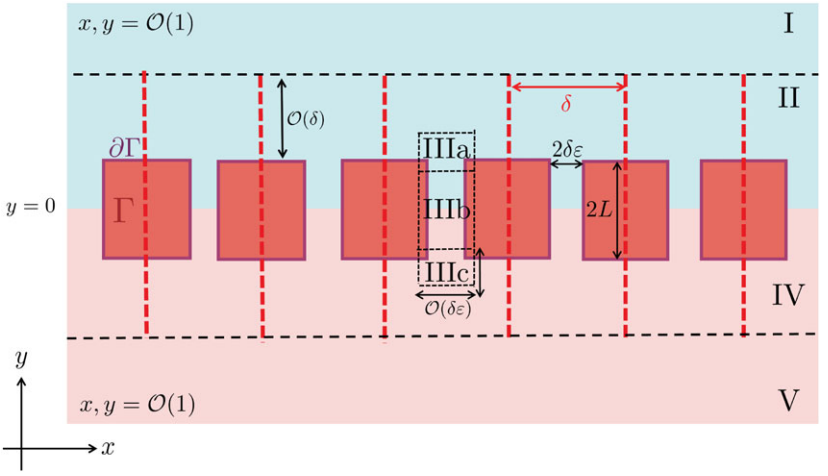

Figure 2. Full asymptotic structure and non-dimensional geometry of the perforated membrane problem in 2D. We show Γ, the impermeable parts of membrane in red, and its boundary, $\partial\Gamma$ in purple, where we apply no flux conditions. Regions I and V denote our outer regions where x and y are of $\mathcal{O}(1)$. Regions II and IV denote the boundary layers on either side of the membrane and regions IIIa, b and c represent our three inner regions. In the $\mathcal{O}(1)$ aspect ratio problem, these collapse to one inner region.

To get an idea of the relative sizes of our non-dimensional parameters, we take, for example, $R^* = 360\,\text{nm}$, $r^* = 10\,\text{nm}$, $a^* = 0.325\,\text{nm}$ and $2L^* = 12\,\text{nm}$ from table 1 giving approximate scalings for our non-dimensional parameters of $\delta = 0.028$, $\varepsilon = 0.0325$ (i.e. $\delta\varepsilon = 0.00091$) and $L = 0.017$. With this choice of physical parameter values, we have $\delta\varepsilon \ll L$ and $\delta, \varepsilon \ll 1$, meaning adjacent channels are close relative to bacterial radius, channel width is small compared to channel spacing and channels are much longer than they are wide, motivating the asymptotic structure we detail below.

(a) Asymptotic structure

We proceed in deriving an effective coupling condition for transport across the membrane by exploiting the disparity in lengthscales within the problem. Specifically, we consider the scenario in which the membrane has many well-separated gaps, i.e. gap width is much smaller than the separation length. Mathematically, the limit of many gaps corresponds to $\delta \ll 1$, and the limit of well separated gaps corresponds to $\varepsilon \ll 1$. From table 1, we see that $L/\delta\varepsilon \approx 1{-}100$. The limit in which $L/\delta\varepsilon = \mathcal{O}(1)$, which we refer to as the $\mathcal{O}(1)$ aspect ratio limit, is of potential physical relevance, and acts as a distinguished limit here, with the 'long thin channel' limit, $\delta\varepsilon \ll L$, emerging as a sublimit of this problem. However, we later demonstrate that the coupling conditions derived in the long thin channel problem work well across most parameters investigated, since this captures transport dominated by channel entrance effects as well as channel length effects. As such, we present the long thin channel limit in the main text, allowing for more straightforward mathematical analysis and more interpretable derived effective coupling conditions. We present the $\mathcal{O}(1)$ aspect ratio limit in appendix A and discuss the key results for this limit in §3d.

In both of the limits described above, our domain has several distinct asymptotic regions in space, as highlighted in figure 2 and detailed in figure 3. In the order we discuss them below, we term these the 'outer', 'boundary' and 'inner' regions. In the outer regions away from the membrane, $x = \mathcal{O}(1)$, and these are the regions we wish to connect via our effective coupling conditions. Our outer regions I and V are shown in figure 3a. We then have boundary layer regions, II and IV, on either side of the membrane where $|y \pm L| = \mathcal{O}(\delta)$. In these regions, the

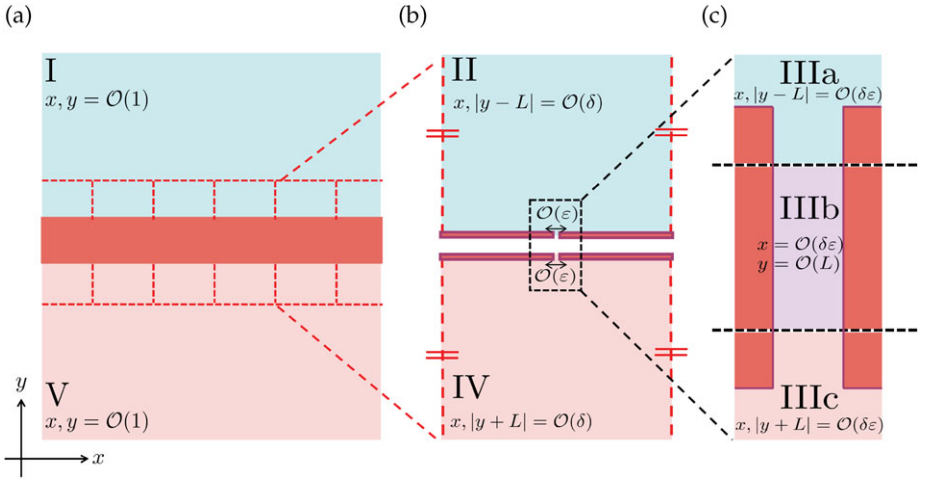

Figure 3. Asymptotic structure of (a) the outer regions, (b) the boundary layer region cell problem and (c) the inner regions of the multiple gaps problem in 2D. In each region, we show the asymptotic size of the (x, y) coordinates.

individual nature of the gaps becomes evident, but we still cannot see their full structure and the gaps act as effective sinks or sources. In these regions, we must analyse a multiple scales problem in x with long-scale variation of $\mathcal{O}(1)$ and short-scale variation of $\mathcal{O}(\delta)$, giving us periodic mathematical 'cells' of $\mathcal{O}(\delta)$ as shown in figure 3b. Our two boundary layer regions are connected by our inner regions labelled IIIa–c where $x = \mathcal{O}(\delta\varepsilon)$, shown in figure 3c. Here, we can see the full finite geometry of the gap. Inner regions IIIa and IIIc describe the $\mathcal{O}(\delta\varepsilon)$ regions about our two gap openings, and inner region IIIb describes the length of the channel where $y = \mathcal{O}(L)$. In the $\mathcal{O}(1)$ aspect ratio limit, IIIa–c coalesce into a single inner region.

3. Steady problem

We start by considering the steady problem, setting the time derivative in equation (2.3*a*) to zero. To determine our effective coupling conditions, we calculate the leading-order concentration in each of our asymptotic regions and then asymptotically match our solutions across each region. This process connects the outer region concentrations, systematically taking into account the variation across the channel owing to geometry. As discussed above, we present the full solution for the long thin channel limit $\delta\varepsilon \ll L$.

For convenience, we first analyse the inner regions, then the boundary layer regions and finally the outer regions (see figure 3). Our goal is to understand how the flux through these regions depends on the problem geometry and how this information generates an appropriate effective macroscale membrane condition.

(a) Inner regions

We start by considering the three inner regions in our periodic cell, as shown in figure 3c. In these inner problems, we have $x = \mathcal{O}(\delta\varepsilon)$. Starting within the channel and working outwards, we first consider region IIIb, in which concentration diffuses across the length of the channel.

(i) Region IIIb

The first and simplest region is region IIIb where we have $x = \mathcal{O}(\delta\varepsilon)$ and $y = \mathcal{O}(L)$. Although $\delta\varepsilon \ll L$ here, the precise size of L beyond this is not important for our analysis. As it is mathematically convenient to do so, we henceforth formally treat $L = \mathcal{O}(1)$, which does not affect

our leading-order analysis. We scale into region IIIb by defining a rescaled horizontal coordinate

$$x = \delta\varepsilon\bar{X}, \tag{3.1}$$

which transforms equation (2.3) into

$$\frac{\partial^2 c}{\partial \bar{X}^2} + (\delta\varepsilon)^2 \frac{\partial^2 c}{\partial y^2} = 0, \quad |\bar{X}| < 1, |y| < L \tag{3.2a}$$

and

$$\frac{\partial c}{\partial \bar{X}} = 0, \quad |\bar{X}| = 1, |y| < L, \tag{3.2b}$$

where the asymptotic region IIIb is defined via $\{(\bar{X}, y) : |\bar{X}| < 1, |y| < L\}$. At leading order, equations (3.2) imply that $c \sim c(y)$. We determine this leading-order function of y by integrating equation (3.2*a*) over $\bar{X} \in (-1, 1)$ and applying the boundary condition equation (3.2*b*). Hence, the leading-order concentration satisfies

$$\frac{\mathrm{d}^2 c}{\mathrm{d}y^2} = 0, \tag{3.3}$$

effectively corresponding to one-dimensional diffusion through the channel. We may therefore deduce

$$c \sim \alpha y + \beta, \tag{3.4}$$

where the integration constants α and β must be determined by asymptotic matching. We next consider regions IIIa and IIIc, the gap opening region. We emphasize that these smaller asymptotic regions terminate region IIIb at finite values of y, rather than transitioning at asymptotically large values of y.

(ii) Regions IIIa and IIIc

We now investigate region IIIc, which is defined by an $\mathcal{O}(\delta\varepsilon)$ region about the gap opening centred at $\boldsymbol{x} = (0, -L)$. The analysis for region IIIa follows from the region IIIc analysis immediately from symmetry. We scale into region IIIc defining rescaled horizontal and vertical coordinates:

$$x = \delta\varepsilon\bar{X}, \quad y = -L + \delta\varepsilon Y_-, \tag{3.5}$$

converting equation (2.3) into the following scaled system:

$$0 = \frac{\partial^2 c}{\partial \bar{X}^2} + \frac{\partial^2 c}{\partial Y_-^2}, \quad \{\bar{X} \in \mathbb{R}, Y_- < 0\} \cup \{|\bar{X}| < 1, Y_- > 0\} \tag{3.6a}$$

and

$$\frac{\partial c}{\partial n} = 0, \quad \{|\bar{X}| > 1, Y_- = 0\} \cup \{|\bar{X}| = 1, Y_- > 0\}. \tag{3.6b}$$

Although we are formally considering an asymptotic series expansion of our concentration, only the leading-order problem will be relevant for our purposes here, so we work directly with equations (3.6).

As equation (3.6*a*) represents Laplace's equation in a 2D domain, we use conformal mapping to map our region IIIc problem into a domain in which it is easier to solve. Specifically, setting $Z_- = \bar{X} + iY_-$, we use the combination of a Schwarz–Christoffel map from the upper-half-plane to the open polygon representing our physical domain and a map from the upper-half-plane to an infinite strip, in which our problem is straightforward to solve [42]. These two maps are shown schematically in figure 4. Our Schwarz–Christoffel map from the upper-half-plane to the physical domain takes the form

$$Z_- = -1 - \frac{2}{\pi}\left((\omega_-^2 - 1)^{1/2} - \frac{1}{2i}\log\left(\frac{i - (\omega_-^2 - 1)^{1/2}}{i + (\omega_-^2 - 1)^{1/2}}\right)\right), \tag{3.7}$$

where we chose the branch cuts to lie outside our physical domain for the complex logarithm and square-root functions.

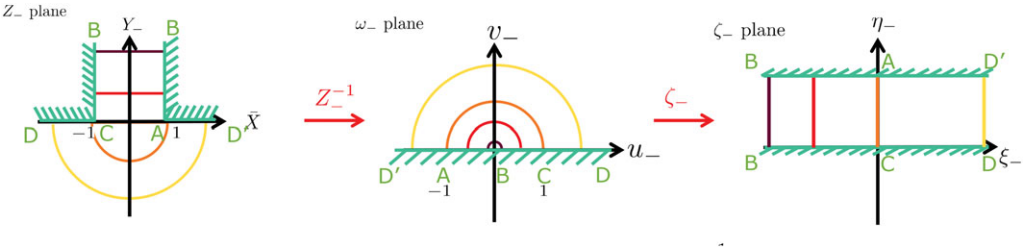

Figure 4. Schematic to show the effects of the conformal maps Z_-^{-1}, equation (3.7), and ζ_-, equation (3.8), on the physical domain, with contour lines to show how the space is transformed.

Combining equation (3.7) with the standard map from the upper-half-plane to the semi-infinite strip

$$\zeta_- = \frac{2}{\pi}\log\omega_-, \tag{3.8}$$

where $\zeta_- = \xi_- + i\eta_-$, we can write the full transformation from the semi-infinite strip to our physical domain as

$$Z_- = -1 - \frac{2}{\pi}\left((e^{\pi\zeta_-}-1)^{1/2} - \frac{1}{2i}\log\left(\frac{i-(e^{\pi\zeta_-}-1)^{1/2}}{i+(e^{\pi\zeta_-}-1)^{1/2}}\right)\right). \tag{3.9}$$

In the semi-infinite strip, our problem is now given by

$$\frac{\partial^2 c}{\partial\eta_-^2} + \frac{\partial^2 c}{\partial\xi_-^2} = 0, \quad \{\xi_- \in \mathbb{R}, 0 < \eta_- < 2\} \tag{3.10a}$$

and

$$\frac{\partial c}{\partial\eta_-} = 0, \quad \eta_- = 0, 2. \tag{3.10b}$$

Our remaining task is to find solutions to Laplace's equation with a finite flux through the channel region. In the transformed ζ_- plane, the general solution corresponding to a finite flux is $c \sim a_-\mathrm{Re}\zeta_- + b_-$, which can be simply transformed into the ω_- plane using equation (3.8):

$$c \sim \frac{2}{\pi}a_-\mathrm{Re}(\log\omega_-) + b_-, \tag{3.11}$$

where a_- and b_- are constants to be determined via later matching.

For these matching purposes, it is helpful to record various far-field behaviours. From the form of the transformation equation (3.7), we may deduce that

$$Z_- \sim -\frac{2}{\pi}\omega_- \to -\infty \quad \text{as } |\omega_-| \to \infty. \tag{3.12}$$

Therefore, combining equations (3.11) and (3.12), we have

$$c \sim \frac{2a_-}{\pi}\log|Z_-| + \frac{2a_-}{\pi}\log\frac{\pi}{2} + b_- \quad \text{as } |Z_-| \to \infty, Y_- < 0. \tag{3.13}$$

Similarly, from equation (3.7), we deduce that

$$Z_- \sim -1 - \frac{2i}{\pi} - \frac{2i}{\pi}\log\omega_- + \frac{2i}{\pi}\log 2 \quad \text{as } \omega_- \to 0, \tag{3.14}$$

and then combining equations (3.11) and (3.14), we have

$$c \sim -a_-Y_- - \frac{2a_-}{\pi} + \frac{2a_-}{\pi}\log 2 + b_- \quad \text{as } Z_- \to i\infty. \tag{3.15}$$

As noted above, the analysis for region IIIa follows immediately via symmetry. Very briefly, we scale into this region using

$$x = \delta\varepsilon\bar{X} \quad \text{and} \quad y = L + \delta\varepsilon Y_+. \tag{3.16}$$

Setting $Z_+ = \bar{X} + iY_+$, the equivalent map taking the semi-infinite strip in the ζ_+ plane to the physical Z_+-plane is

$$Z_+ = 1 + \frac{2}{\pi}\left((e^{\pi\zeta_+} - 1)^{1/2} - \frac{1}{2i}\log\left(\frac{i - (e^{\pi\zeta_+} - 1)^{1/2}}{i + (e^{\pi\zeta_+} - 1)^{1/2}}\right)\right). \tag{3.17}$$

Hence, our solution in region IIIa is

$$c \sim a_+ \mathrm{Re}(\zeta_+) + b_+, \tag{3.18}$$

where a_+ and b_+ are determined by later asymptotic matching, and ζ_+ is our intermediate variable describing the semi-infinite strip. In this case, the far-field behaviour takes the forms

$$c \sim \frac{2a_+}{\pi}\log|Z_+| + \frac{2a_+}{\pi}\log\frac{\pi}{2} + b_+ \quad \text{as } |Z_+| \to \infty, Y_+ > 0 \tag{3.19a}$$

and

$$c \sim a_+ Y_+ - \frac{2a_+}{\pi} + \frac{2a_+}{\pi}\log 2 + b_+ \quad \text{as } Z_+ \to -i\infty. \tag{3.19b}$$

We have now determined the solutions in the three inner regions. Our remaining tasks are (i) to derive the leading-order concentration in the boundary layer regions, where the individual nature of the channels is apparent as point sinks or sources, and (ii) match between all the asymptotic regions to obtain the effective coupling conditions we seek.

(b) Boundary layers: regions II and IV

As with our inner regions, the analysis for region II follows from the region IV analysis via symmetry. Region IV arises when $y = \mathcal{O}(\delta)$ with $y < -L$ as shown in figure 3b. The local periodicity of this problem means that this takes the form of a multiple scales problem in x where we have periodic delta sinks or sources situated at δj for $j \in \mathbb{Z}$ on an otherwise impermeable line. We choose our coordinates so that the centre of one gap lies on $\boldsymbol{x} = \mathbf{0}$, and scale into our periodic cell-level problem on this gap centred at the origin, using the scaling

$$y = -L + \delta Y_1, \tag{3.20}$$

and introducing the microscale variable

$$X = \frac{x}{\delta}. \tag{3.21}$$

In the standard multiple scales manner, we assume that x and X are independent of one another, considering $c = c(x, X, Y_1)$. To remove the extra degree of freedom this introduces, we impose periodicity in X. The symmetry of the geometry means that this periodicity is equivalent to imposing no flux boundary conditions on the periodic boundaries of our cell.

To match the region IIIa and IIIc solutions, equations (3.11) and (3.18), into our boundary layer regions II and IV, we have to match the flux from the inner problems through regions of $\mathcal{O}(\varepsilon)$ in the boundary layer problems. To facilitate this matching, we introduce delta functions in the leading-order boundary layer problems, representing the inner regions as effective point sinks or sources. The strength of these effective delta functions will be related to the microscale channel geometry and flux through later matching.[1]

[1]A strictly formal asymptotic matching procedure would require writing c as an asymptotic expansion and taking care about the asymptotic strength of the delta function. However, since we are able to solve the problem with an $\mathcal{O}(1)$-strength delta function, it is more straightforward to solve this general problem without considering relative strengths, and then to determine the precise strength of the delta function *a posteriori* via matching.

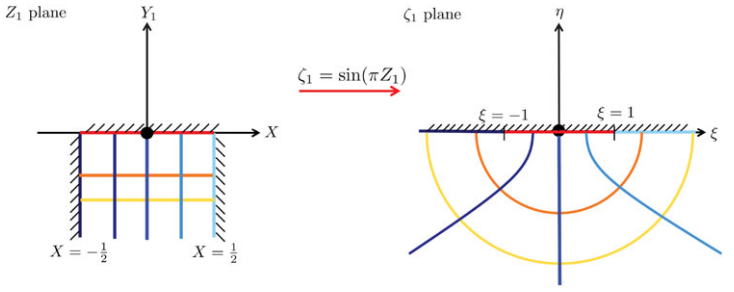

Figure 5. Cell-level region IV under the mapping equation (3.23) showing the transformation of lines of constant X and Y_1.

The leading-order problem in region IV is therefore

$$\nabla^2_{B1}c=0,\quad Y_1<0,\ -\frac{1}{2}<X<\frac{1}{2}, \tag{3.22a}$$

$$\frac{\partial c}{\partial Y_1}=\kappa_1\hat{\delta}(X,Y_1)=\kappa_1\hat{\delta}(X),\quad Y_1=0,\ -\frac{1}{2}<X<\frac{1}{2} \tag{3.22b}$$

and

$$\frac{\partial c}{\partial X}=0,\quad Y_1<0,\ X=\pm\frac{1}{2}, \tag{3.22c}$$

where we denote $\nabla^2_{B1}:=(\partial^2/\partial X^2)+(\partial^2/\partial Y_1^2)$ to represent the Laplacian purely in microscale variables. Here, $\hat{\delta}$ is the Dirac delta function introduced for matching purposes as discussed above, and κ_1 is the (as-of-yet unknown) strength of the effective source/sink given by the flux, determined later via matching. We have replaced the condition of periodicity in X with a no flux condition, which is equivalent owing to the symmetric geometry of this cell problem. Setting $Z_1=X+iY_1$, we use the standard conformal map

$$\zeta_1=\sin(\pi Z_1) \tag{3.23}$$

to map our open box domain to the lower half-plane, as shown in figure 5.

In the ζ_1 plane, equations (3.22) become

$$\nabla^2_{\zeta 1}c=0,\quad \eta<0,\xi\in\mathbb{R} \tag{3.24a}$$

and

$$\frac{\partial c}{\partial \eta}=\kappa_1\hat{\delta}(\xi,\eta)=\kappa_1\hat{\delta}(\xi),\quad \eta=0,\xi\in\mathbb{R}, \tag{3.24b}$$

where we denote $\nabla^2_{\zeta 1}:=(\partial^2/\partial\xi^2)+(\partial^2/\partial\eta^2)$. Using Neumann–Green's functions [43], equations (3.24) are solved by

$$c=A_1+\frac{\kappa_1}{2\pi}\log(\eta^2+\xi^2)=A_1+\frac{\kappa_1}{\pi}\log|\zeta_1|=\frac{\kappa_1}{\pi}\mathrm{Re}(\log(\zeta_1)), \tag{3.25}$$

where A_1 and κ_1 are constants that will be determined from matching later. Hence, our region IV solution is

$$c\sim A_1+\frac{\kappa_1}{\pi}\mathrm{Re}(\log(\sin(\pi Z_1))). \tag{3.26}$$

The analysis in region II follows from that in region IV by symmetry. The appropriate scaling in this case is

$$y=L+\delta Y_2 \tag{3.27}$$

and, using the notation $Z_2=X+iY_2$, is solved by

$$c\sim A_2+\frac{\kappa_2}{\pi}\mathrm{Re}(\log(\zeta_2))=A_2+\frac{\kappa_2}{\pi}\mathrm{Re}(\log(\sin(\pi Z_2))), \tag{3.28}$$

where A_2 and κ_2 are determined from later matching. This concludes our specific analysis of all inner and boundary regions. It is useful to determine the limiting forms of equations (3.28) and

(3.26) as $Y_i \to \mp\infty$ and $|Z_i| \to 0_{\mp}$, $i \in \{1,2\}$, for later matching purposes. First, taking the limit as $Y_i \to \pm\infty$, we obtain

$$c \sim A_i \mp \kappa_i Y_i - \frac{\kappa_i}{\pi}\log 2 \quad \text{as } Y_i \to \mp\infty, \quad i \in \{1,2\}, \tag{3.29}$$

which we use to match into the outer regions. Next, taking the limit as $|Z_i| \to 0_{\mp}$, we obtain

$$c \sim A_i + \frac{\kappa_i}{\pi}\log|\pi Z_i| \quad \text{as } |Z_i| \to 0_{\mp}, \quad i \in \{1,2\}, \tag{3.30}$$

which we match to our inner region solutions.

(c) Effective coupling conditions for the long thin channel limit

Our final task for the steady problem is to match our solutions between each asymptotic region. This generates the asymptotically correct connection formulae between the outer concentrations and concentration fluxes, which are the effective coupling conditions we have been seeking. We match from our outer regions inwards, allowing us to determine our unknown constants in each region entirely in terms of outer quantities. First, Taylor expanding the outer solutions about $y = \pm L$, we obtain

$$c(x,y) = c(x,\pm L + \delta Y_i) \sim c|_{\pm L} + \delta Y_i \frac{\partial c}{\partial y}|_{\pm L}, \quad i \in \{1,2\}. \tag{3.31}$$

Matching our outer solutions equation (3.31), to our regions II and IV solutions in the limit $Y_i \to \mp\infty$, $i \in \{1,2\}$, equation (3.29), we deduce that

$$\kappa_1 = -\delta \frac{\partial c}{\partial y}|_{y=-L} \quad \text{and} \quad \kappa_2 = \delta \frac{\partial c}{\partial y}|_{y=L} \tag{3.32a}$$

and

$$A_1 = c|_{y=-L} - \frac{\delta}{\pi}\frac{\partial c}{\partial y}|_{y=-L}\log 2 \quad \text{and} \quad A_2 = c|_{y=L} + \frac{\delta}{\pi}\frac{\partial c}{\partial y}|_{y=L}\log 2. \tag{3.32b}$$

Similarly matching our regions IIIa and IIIc solutions as $Z_{\mp} \to \mp\infty$, equations (3.19*a*) and (3.13), to our regions II and IV solutions in the limit $Z_i \to 0$, $i \in \{1,2\}$, equation (3.30), we obtain

$$2a_- = \kappa_1 \quad \text{and} \quad 2a_+ = \kappa_2 \tag{3.33a}$$

and

$$b_- = A_1 + \frac{\kappa_1}{\pi}\log 2\varepsilon \quad \text{and} \quad b_+ = A_2 + \frac{\kappa_2}{\pi}\log 2\varepsilon. \tag{3.33b}$$

Finally, matching the solutions in regions IIIa and IIIc, equations (3.19*b*) and (3.15), to the solution in region IIIb, equation (3.4), we obtain relations between a_-, a_+, b_- and b_+:

$$\alpha = -\frac{a_-}{\delta\varepsilon} = \frac{a_+}{\delta\varepsilon} \quad \text{and} \quad \beta = b_- + \alpha L + \frac{2a_-}{\pi}(\log 2 - 1) = b_+ - \alpha L + \frac{2a_+}{\pi}(\log 2 - 1). \tag{3.34}$$

Substituting equations (3.32) into (3.33), we can write $a_{\pm}, b_{\pm}$ in terms of the outer concentration, concentration flux and membrane geometry parameters. Subsequently using equation (3.34), which gives us the relationship between $a_{\pm}, b_{\pm}$, we arrive at our effective coupling conditions, directly relating the outer flux and concentrations on either side of the membrane via the classic permeability equation

$$\frac{\partial c}{\partial y}|_{y=-L} = \frac{\partial c}{\partial n}|_{y=L} = P_{\text{eff}}\,[c]_{-L}^{L} \tag{3.35a}$$

and

$$P_{\text{eff}} = \frac{1}{L/\varepsilon + (2\delta/\pi)(\log(1/8\varepsilon) + 1)}. \tag{3.35b}$$

The effective coupling conditions equations (3.35) have the same functional form as equation (1.1), but now with an explicit expression for the effective permeability P_{eff}, equation (3.35*b*), as a function of the physical gap properties of length, width and separation distance. This allows us to directly understand how changing microscale geometry affects membrane permeability,

and hence the concentration jump across the membrane. Continuity of flux is encoded in equation (3.35*a*) (and equation (1.1)), which follows physically since flux is conserved throughout the inner regions. We validate equations (3.35) against numerical simulations of the full membrane geometry in §5.

(d) The $\mathcal{O}(1)$ aspect ratio limit

We present the $\mathcal{O}(1)$ aspect ratio limit, where $\delta\varepsilon = \mathcal{O}(L)$, in detail in appendix A, summarizing the main results here. We introduce the channel aspect ratio $a = L/\delta\varepsilon = \mathcal{O}(1)$ for notational convenience. Briefly, the main change from our analysis above is that our inner regions IIIa, IIIb and IIIc coalesce into a single inner region encompassing the gap openings and length. We can solve this problem using a different complex variable mapping to transform our gap domain to the upper-half-plane; that is, the inverse of the conformal map:

$$Z = X + iY = ai + d\left\{\omega\left(1-\frac{1}{\omega^2}\right)^{1/2}\left(1-\frac{\lambda^2}{\omega^2}\right)^{1/2} - E\left(\arcsin\frac{1}{\omega},\lambda\right) - \lambda E\left(\arcsin\frac{\lambda}{\omega},\frac{1}{\lambda}\right)\right\}, \tag{3.36}$$

where $\{X, Y\} = \{x, y\}/\delta\varepsilon$ are our inner variables describing the new region III, $\omega = u + iv$, $v > 0$, is our mapping variable in the upper-half-plane as in equation (3.7), and $E(\phi, k)$ is the incomplete elliptic integral of the second kind defined by

$$E(\phi, k) = \int_0^{\sin\phi} \frac{\sqrt{1-k^2t^2}}{\sqrt{1-t^2}}\,\mathrm{d}t. \tag{3.37}$$

As in equation (3.7), we choose the branch cuts for equation (3.36) to lie outside the physical domain. The constant d is defined as

$$d = -\frac{1}{\{E(\arcsin 1/\lambda, \lambda) + \lambda E(\pi/2, 1/\lambda)\}} \in \mathbb{R}, \tag{3.38}$$

where the constant $\lambda(a) > 1$ is defined implicitly through the relation

$$2a = \left(\int_1^\lambda \frac{(\lambda^2 - t^2)^{1/2}}{(t^2-1)^{1/2}}\,\mathrm{d}t - \lambda\int_{1/\lambda}^1 \frac{(t^2 - (1/\lambda^2))^{1/2}}{(1-t^2)^{1/2}}\,\mathrm{d}t\right) \times \left(\int_0^1 \frac{(\lambda^2 - t^2)^{1/2}}{(1-t^2)^{1/2}}\,\mathrm{d}t - \lambda\int_0^{1/\lambda} \frac{((1/\lambda^2) - t^2)^{1/2}}{(1-t^2)^{1/2}}\,\mathrm{d}t\right)^{-1}, \tag{3.39}$$

noting that $\lambda \to 1$ as $a \to 0$. Proceeding as before, we use the limiting behaviour of the solution and the map equation (3.36) to match into our boundary layer regions. This procedure yields our effective coupling conditions, which again take the form of the classic permeability equation (1.1), but now P_{eff} is given by

$$P_{\text{eff}} = \frac{1}{\delta/\pi\,\log(1/4\varepsilon^2\pi^2\lambda d^2)}. \tag{3.40}$$

We now investigate how the effective permeability changes in this $O(1)$ aspect ratio limit, equation (3.40), compared to the long thin limit, equation (3.35*b*). To do this, we examine the dependence of λ on a, written implicitly in equation (3.39) and plotted in figure 6*a*. We see that $a \to 0$ corresponds to $\lambda \to 1$ and $a \to \infty$ corresponds to $\lambda \to \infty$. As such, we now examine the leading-order approximations of the integrals in equation (3.39) in the limits $\lambda \to 1$ and $\lambda \to \infty$.

We first explore how a small aspect ratio affects the form of the effective permeability by taking the limit $\lambda \to 1$ (and therefore $a \to 0$) in equation (3.39) to obtain

$$a \sim \frac{\pi}{16}(\lambda - 1)^2 \quad \text{as } a \to 0 \tag{3.41}$$

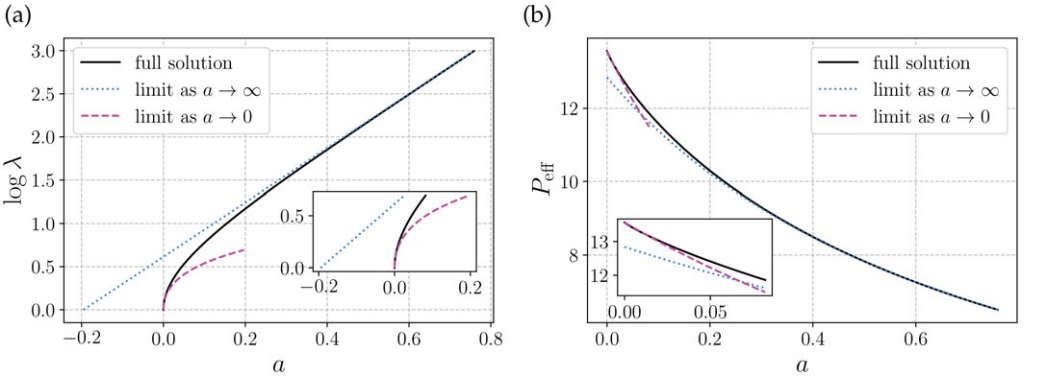

Figure 6. (a) Aspect ratio $a = L/\delta\varepsilon$ versus λ as given by equation (3.39). We include the leading-order term in the expansion as $a \to 0$, equation (3.41) (pink), alongside the leading-order expansion as $a \to \infty$, equation (3.43) (blue). (b) Aspect ratio $a = L/\delta\varepsilon$ versus P_{eff} as given by equation (3.40). We include the leading-order limiting forms as $a \to 0$, equation (3.42) (pink), and $a \to \infty$, equation (3.44) (blue). Inset plots show behaviour for small a.

to leading order. Substituting equation (3.41) into equation (3.40), we deduce

$$P_{\text{eff}} \sim \frac{1}{2\delta/\pi \log(1/\varepsilon\pi) + (16/\pi^2)\delta a} \sim \frac{1}{2\delta/\pi \log 1/\varepsilon\pi} \quad \text{as } a \to 0, \tag{3.42}$$

where we have used $d \sim -1/2 + (\lambda - 1)/4$ as $\lambda \to 1$ in equation (3.38). We note that in this limit, we require ε sufficiently small, $\varepsilon \ll \exp(-1/\delta)$, to sustain a leading-order concentration difference across the membrane. For larger ε, we find $P_{\text{eff}} \to \infty$ and we recover the results in [20], where concentration is equal on either side of an infinitely thin membrane at leading order. Similarly, we explore the large-aspect-ratio limit by taking $\lambda \to \infty$ (and therefore $a \to \infty$) in equation (3.39) to obtain

$$a \sim \frac{1}{\pi}(\log 4\lambda - 2) \quad \text{as } a \to \infty. \tag{3.43}$$

Substituting equation (3.43) into equation (3.40), we now obtain

$$P_{\text{eff}} \sim \frac{1}{2\delta/\pi(\log(1/8\varepsilon) + 1) + a\delta} \quad \text{as } a \to \infty, \tag{3.44}$$

using $d \sim -2/\pi\lambda$ as $\lambda \to \infty$ in equation (3.38). Writing $a = L/\delta\varepsilon$, we find that the large-a limit of the $O(1)$ aspect ratio permeability equation (3.44) recovers the effective permeability equation (3.35*b*) we derived separately from our long thin channel limit analysis. We note that the effective permeability in both small and large aspect ratio limits, equations (3.42) and (3.44), depends on the membrane geometry through the parameters a, δ and ε with the same functional form, but with different pre-multiplying constants.

In figure 6b, we show how the effective permeability, P_{eff}, varies with the aspect ratio, $a = L/\delta\varepsilon$, including the full effective permeability in our $\mathcal{O}(1)$ aspect ratio limit, equation (3.40) and the two limiting forms equations (3.42) and (3.44). We see that the large aspect ratio limit matches well even as the aspect ratio becomes fairly small, with good agreement for $a \gtrsim 0.25$, meaning that our simpler long thin channel limit performs well as an effective interface condition unless the membrane is much thinner than the width of the gaps.

4. Time-dependent problem

We now return to the full unsteady problem. Importantly, the genuine unsteady nature of the problem for $t = \mathcal{O}(1)$ is only relevant for the upscaling procedure in the long thin channel limit. This is because the small lengthscales in the boundary layer and inner regions lead to quick equilibration in the $\mathcal{O}(1)$ aspect ratio limit, and so equations (1.1) and (3.40) would still hold,

albeit in a quasi-steady manner. However, in the long thin channel limit, the channel length L can be large enough so that in region IIIb, transport across the channel is not quasi-steady. As we shall see, this introduces additional technicalities and emergent effects when deriving effective coupling conditions. Specifically, we find that the coupling conditions we derive gain memory properties, where the history of the system becomes important. Given that the only significant change between analysis in the time-dependent problem is in region IIIb, we focus on this region below.

(a) Region IIIb

As before, region IIIb describes the channel, where $x = \mathcal{O}(\delta\varepsilon)$ and $y = \mathcal{O}(L)$. We scale into this region using

$$x = \delta\varepsilon\bar{X} \quad \text{and} \quad y = -L + 2\bar{y}, \tag{4.1}$$

where our y scaling is chosen for later notational convenience. Our channel is now defined by $\{(\bar{X}, \bar{y}) : |\bar{X}| < 1, 0 < \bar{y} < L\}$. Substituting the scalings equation (4.1) into our unsteady system equation (2.3) for our channel region, we obtain

$$(\delta\varepsilon)^2 \frac{\partial c}{\partial t} = \frac{\partial^2 c}{\partial \bar{X}^2} + \frac{(\delta\varepsilon)^2}{4} \frac{\partial^2 c}{\partial \bar{y}^2}, \quad |\bar{X}| < 1,\ 0 < \bar{y} < L \tag{4.2a}$$

and

$$\frac{\partial c}{\partial \bar{X}} = 0, \quad |\bar{X}| = 1,\ 0 < \bar{y} < L. \tag{4.2b}$$

In the same manner as in §3a(i), we deduce that the leading-order concentration is independent of $\bar{X}$, so now we have $c \sim c(y, t)$, and hence the leading-order concentration satisfies

$$\frac{\partial c}{\partial t} \sim \frac{1}{4} \frac{\partial^2 c}{\partial \bar{y}^2}, \quad 0 < \bar{y} < L. \tag{4.3}$$

We can write the general solution of equation (4.3) as

$$c(\bar{y}, t) \sim \alpha(t)\bar{y} + \beta(t) + \sum_{n=1}^{\infty} g_n(t) \sin \lambda_n \bar{y} \quad \text{and} \quad \lambda_n = \frac{n\pi}{L}, \tag{4.4}$$

where the functions $\alpha(t)$ and $\beta(t)$ are the time-dependent analogues to the constants of integration in the steady problem equation (3.4), and will be determined via later matching with the other regions. As we shall see later, the functions $g_n(t)$ represent genuinely unsteady effects, and splitting the solution as in equation (4.4) generates helpful smoothness properties whereby the $\bar{y}$-derivative of the infinite sum in equation (4.4) is convergent.

Substituting equation (4.4) into equation (4.3), multiplying by $\sin \lambda_m \bar{y}$ and integrating over $\bar{y}$ in $(0, L)$, we obtain the following ordinary differential equation (ODE) for each $g_n(t)$:

$$\frac{\mathrm{d}}{\mathrm{d}t} g_n + \frac{\lambda_n^2}{4} g_n = \frac{\mathrm{d}}{\mathrm{d}t} \left(\frac{2\alpha}{\lambda_n} (-1)^n + \frac{2\beta}{L\lambda_n} ((-1)^n - 1) \right). \tag{4.5}$$

Solving the linear ODE equation (4.5) using standard methods, we obtain the solution

$$\begin{aligned} g_n(t) = \exp\left(-\frac{\lambda_n^2 t}{4}\right) g_n(0) + \exp\left(-\frac{\lambda_n^2 t}{4}\right) \int_0^t \exp\left(\frac{\lambda_n^2 \tau}{4}\right) \\ \times \frac{\mathrm{d}}{\mathrm{d}\tau} \left(\frac{2\alpha(\tau)}{\lambda_n} (-1)^n + \frac{2\beta(\tau)}{L\lambda_n} ((-1)^n - 1) \right) \mathrm{d}\tau. \end{aligned} \tag{4.6}$$

Reassuringly, $g_n(t) \to 0$ as $t \to \infty$ if $\mathrm{d}\alpha/\mathrm{d}t, \mathrm{d}\beta/\mathrm{d}t \to 0$ as $t \to \infty$, from which we can recover the steady equation (3.4).

Returning to the time-dependent solution equation (4.6), with initial condition represented by $c_{\text{init}}(\bar{y})$ in the channel length, and writing in terms of a Fourier series, we have

$$g_n(0) = \frac{2\alpha(0)}{\lambda_n}(-1)^n + \frac{2\beta(0)}{L\lambda_n}((-1)^n - 1) + \frac{2}{L}\int_0^L c_{\text{init}}(\bar{y}) \sin \lambda_n \bar{y}\, \mathrm{d}\bar{y}. \tag{4.7}$$

For brevity, we henceforth set $c_{\text{init}}(\bar{y}) = 0$, but it is straightforward to extend the following to general initial conditions if required.

Our final task is to match our solutions to determine $\alpha(t)$ and $\beta(t)$ in terms of outer variables. This gives us the effective coupling conditions we seek by formally connecting the outer variables on either side of the membrane.

(b) Time-dependent effective coupling conditions

As time only arises as an effective parameter in the boundary layer and region IIIa and IIIc solutions, the matching between those regions is essentially the same as for the steady case. This generates the relations (3.32) and (3.33), but with matching functions of time $\kappa_{1,2}$, $A_{1,2}$, $a_\pm$ and $b_\pm$ instead of parameters. The fundamental difference in the unsteady problem is the explicit time dependence in region IIIb. This means that the matching between region IIIb and its neighbouring regions IIIa and IIIc needs to be considered separately, which we discuss below.

To match, it is helpful to expand equation (4.4), our solution in region IIIb, in terms of its derivatives. We expand equation (4.4) about $\bar{y} = 0$ and $\bar{y} = L$, using the regions IIIa and IIIc scalings, $Y_\pm$, equations (3.5) and (3.16), to obtain

$$c(\bar{y}, t) \sim c(\bar{y} = 0; t) + \frac{\delta\varepsilon}{2} Y_- \frac{\partial c}{\partial \bar{y}}(\bar{y} = 0; t) \quad \text{as } \bar{y} \to 0 \tag{4.8a}$$

and

$$c(\bar{y}, t) \sim c(\bar{y} = L; t) + \frac{\delta\varepsilon}{2} Y_+ \frac{\partial c}{\partial \bar{y}}(\bar{y} = L; t) \quad \text{as } \bar{y} \to L. \tag{4.8b}$$

We match into regions IIIa and IIIc using the values of the region IIIb concentrations and concentration fluxes at the region IIIb endpoints.

Matching regions IIIa and IIIc with their respective outer regions follows in a similar manner to §3c. We can therefore expand our leading-order solutions in regions IIIa and IIIc, equations (3.11) and (3.18), as they approach the channel entrance, to obtain

$$c \sim c_\mp \pm \frac{\delta}{\pi}\frac{\partial c_\mp}{\partial y}\left(1 + \log\frac{1}{8\varepsilon}\right) + \frac{\delta}{2}\frac{\partial c_\mp}{\partial y} Y_\mp, \qquad Y_\mp \to 0^\mp, \tag{4.9}$$

where for notational convenience, we have introduced the representations $c_\pm := c(y = \pm L, t)$. Comparing equation (4.9) with equations (4.8), we deduce the values of $\alpha(t)$ and $\beta(t)$ in equation (4.4):

$$\alpha(t) = \frac{1}{L}[c]_-^+ - \frac{\delta}{L\pi}\left(1 + \log\frac{1}{8\varepsilon}\right)\left(\frac{\partial c_+}{\partial y} + \frac{\partial c_-}{\partial y}\right) \tag{4.10a}$$

and

$$\beta(t) = c_- + \frac{\delta}{\pi}\left(1 + \log\frac{1}{8\varepsilon}\right)\frac{\partial c_-}{\partial y}. \tag{4.10b}$$

We are now able to write our concentration in region IIIb purely in terms of the membrane microstructure and outer concentration and flux using equations (4.10). We do this using the concentration flux at the endpoints of our channel to obtain our coupling conditions connecting the concentration and flux on either side of the membrane. We start by differentiating equation (4.4) with respect to $\bar{y}$ and evaluate for the flux at the endpoints of our channel using equation (4.6). We then match this with the flux from regions IIIa and IIIc, as given by

equation (4.9), to obtain

$$\frac{\partial c_-}{\partial y} = \varepsilon\alpha(t) + \varepsilon\sum_{n=1}^{\infty}\lambda_n g_n(t) \quad \text{and} \quad \frac{\partial c_+}{\partial y} = \varepsilon\alpha(t) + \varepsilon\sum_{n=1}^{\infty}\lambda_n g_n(t)(-1)^n. \tag{4.11}$$

To obtain our effective interface conditions, we combine equation (4.11) using equations (4.10), relating the average flux and flux jump across the interface. First, the difference between the expressions in equation (4.11) yields

$$\frac{\partial c_+}{\partial y} - \frac{\partial c_-}{\partial y} = \varepsilon\sum_{n\ \text{odd}}\exp\left(-\frac{\lambda_n^2 t}{4}\right)\left\{-2\lambda_n g_n(0) + 4\int_0^t F_n\left(\tau, c_+ + c_-, \frac{\partial c_+}{\partial y} - \frac{\partial c_-}{\partial y}\right)\mathrm{d}\tau\right\} \tag{4.12a}$$

and

$$F_n\left(\tau, c_+ + c_-, \frac{\partial c_+}{\partial y} - \frac{\partial c_-}{\partial y}\right) := \exp\left(\frac{\lambda_n^2\tau}{4}\right)\frac{d}{d\tau}\left(\frac{c_+ + c_-}{L} - \frac{\delta}{\pi L}\left(\log\frac{1}{8\varepsilon} + 1\right)\left(\frac{\partial c_+}{\partial y} - \frac{\partial c_-}{\partial y}\right)\right). \tag{4.12b}$$

Importantly, equations (4.12) represent the first main result from the time-dependent analysis: the time-dependent flux jump across the interface. We note that the infinite sum vanishes and equations (4.12) tend to the steady condition of flux continuity $[\partial c/\partial y]_-^+ = 0$ for large time if $c_\pm$ and $\partial c_\pm/\partial y$ become independent of time as $t \to \infty$.

We obtain the final coupling condition, the average flux across the interface, by summing the expressions in equation (4.11) to arrive at

$$\frac{1}{2}\left(\frac{\partial c_+}{\partial y} + \frac{\partial c_-}{\partial y}\right) = P_{\text{eff}}[c]_-^+ + LP_{\text{eff}}\sum_{n\ \text{even}}\exp\left(-\frac{\lambda_n^2 t}{4}\right) \times\left[\lambda_n g_n(0) + 2\int_0^t G_n\left(\tau, c_+ - c_-, \frac{\partial c_+}{\partial y} + \frac{\partial c_-}{\partial y}\right)\mathrm{d}\tau\right] \tag{4.13a}$$

and

$$G_n\left(\tau, c_+ - c_-, \frac{\partial c_+}{\partial y} + \frac{\partial c_-}{\partial y}\right) := \exp\left(\frac{\lambda_n^2\tau}{4}\right)\frac{\mathrm{d}}{\mathrm{d}\tau}\left(\frac{c_+ - c_-}{L} - \frac{\delta}{\pi L}\left(\log\frac{1}{8\varepsilon} + 1\right)\left(\frac{\partial c_+}{\partial y} + \frac{\partial c_-}{\partial y}\right)\right), \tag{4.13b}$$

where P_{eff} is our steady effective permeability derived in the long thin channel limit, equation (3.35*b*). Equations (4.13) represent the second main result from our time-dependent analysis. This closes the time-dependent problem. We again note that the infinite sum vanishes if $c_\pm$ and $\partial c_\pm/\partial y$ become independent of time as $t \to \infty$, and that in this scenario, equations (4.13) would tend to the steady coupling condition equations (3.35) at large time. We therefore interpret equations (4.13) as our time-dependent effective permeability equation.

The effective unsteady coupling conditions, equations (4.12) and (4.13), represent the key results from our time-dependent analysis. Importantly, these effective coupling conditions have gained a memory property from the time integrals, which is not present in the steady problem. This can be interpreted as a quasi-delay time for information about the environment on one side of the channel to cross to the other side. The importance of this memory contribution depends on the channel geometry, and also the past averages and differences of the concentrations and fluxes, incorporated through the time integral terms. Reassuringly, this memory contribution decays in the large-time limit if the outer concentrations tend to a steady solution; that is, in this scenario, the large-time limits of the sums vanish in equations (4.12) and (4.13) and we recover the steady coupling conditions equations (3.35).

Finally, we also note that the infinite sums in equations (4.12) and (4.13) are slow to converge as $t \to 0^+$. To circumvent this numerical issue, we use an asymptotic Euler–Maclaurin approximation to convert our slowly converging sums into integrals. We present full details

in electronic supplementary material, §1, and note that, assuming vanishing initial conditions for simplicity, the key result of this analysis is that we can write our coupling conditions, equations (4.12) and (4.13), in a simpler closed form as $t \to 0^+$:

$$\frac{\partial c_+}{\partial y} - \frac{\partial c_-}{\partial y} \sim 4\varepsilon L \sqrt{\frac{t}{\pi}} \frac{\mathrm{d}}{\mathrm{d}t} \left[\frac{c_+ + c_-}{L} - \frac{\delta}{\pi L} \left(\log \frac{1}{8\varepsilon} + 1 \right) \left(\frac{\partial c_+}{\partial y} - \frac{\partial c_-}{\partial y} \right) \right] \tag{4.14a}$$

and

$$\frac{1}{2} \left(\frac{\partial c_+}{\partial y} + \frac{\partial c_-}{\partial y} \right) \sim P_{\mathrm{eff}}[c]_-^+ + L^2 P_{\mathrm{eff}} \sqrt{\frac{t}{\pi}} \frac{\mathrm{d}}{\mathrm{d}t} \left[\frac{c_+ - c_-}{L} - \frac{\delta}{\pi L} \left(\log \frac{1}{8\varepsilon} + 1 \right) \left(\frac{\partial c_+}{\partial y} + \frac{\partial c_-}{\partial y} \right) \right]. \tag{4.14b}$$

5. Numerical validation

We now compare simulations of a section of the full membrane problem against simulations with our effective membrane conditions, using the open source finite-element Python package FEniCSx [44–47] with meshes generated using the finite-element mesh generator Gmsh [48]. We take our full domain to have height and width $2R = 5$ in all simulations. In each of our simulations, we impose no flux boundary conditions on the side walls, and Dirichlet boundary conditions on the top and bottom walls of $c = 0$ and $c = 1$, respectively. We validate the numerical method in electronic supplementary material, §3.

(a) Steady simulations

Our simple Neumann and Dirichlet boundary conditions yield an analytic solution to our steady effective problem. Representing our effective permeability as P_{eff} in both the long thin channel limit, equation (3.35*b*), and the $\mathcal{O}(1)$ aspect ratio limit, equation (3.40), we deduce

$$c \sim \begin{cases} 1 - \frac{P_{\mathrm{eff}}\, y}{1 + 2P_{\mathrm{eff}}(R-L)}, & y < R - L, \\ \frac{P_{\mathrm{eff}}(y - 2R)}{1 + 2P_{\mathrm{eff}}(R-L)}, & y > R + L, \end{cases} \tag{5.1}$$

where L is replaced with $a\delta\varepsilon$ in the $\mathcal{O}(1)$ aspect ratio limit.

We focus here on the long thin channel limit (similar results and simulations are obtained in the $\mathcal{O}(1)$ aspect ratio limit). To evaluate the accuracy of our coupling conditions equation (3.35*a*), we take $2L = 0.5$ and vary the number and width of channels between simulations to explore different membrane permeabilities, effectively changing δ and ε.

We obtain good visual agreement between the analytical solutions of our effective interface problem equation (5.1) and simulations of transport in the full geometry, both at higher permeability (figure 7; $\delta = 0.25$, $\varepsilon = 0.25$) and lower permeability (figure 8; $\delta = 0.25$, $\varepsilon = 0.05$). We show the absolute value of the error between the analytical solution of our effective problem and the full simulation in fig. S2 in electronic supplementary material, §2. We plot the flux across a horizontal line away from the membrane in simulations of the full problem alongside our analytical flux calculated from equation (5.1) as we vary permeability in figure 9a. We see good agreement for a range of permeabilities, including for larger permeabilities. For example, the flux predicted by our coupling conditions matches the flux in the full numerical simulation to 99.4% for a membrane with $P_{\mathrm{eff}} = 1.5$, see fig. S1 in electronic supplementary material, §2.

(b) Time-dependent simulations

To evaluate the accuracy of our time-dependent coupling conditions equations (4.12) and (4.13), we carry out our time-dependent simulations using the inbuilt Portable, Extensible Toolkit for Scientific Computation Krylov generalized minimal residual method, with an LU preconditioner, using a time step of $\Delta t = 0.25$ (time step convergence is discussed in electronic supplementary material, §3 and shown in fig. S3b). We plot average flux over a horizontal line away from the

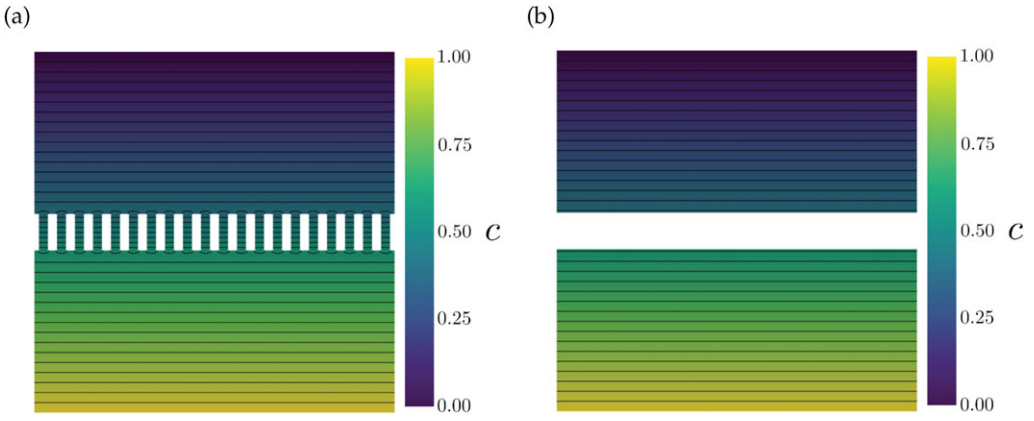

Figure 7. Concentration profile for a membrane with effective permeability $P_{\text{eff}} = 0.953$ and microscale parameters $\delta = 0.25$, $\varepsilon = 0.25$ for (a) a numerical simulation of the full membrane geometry and (b) the analytical solution with our effective interface condition equation (3.35*a*). Contours denote separations of 0.025.

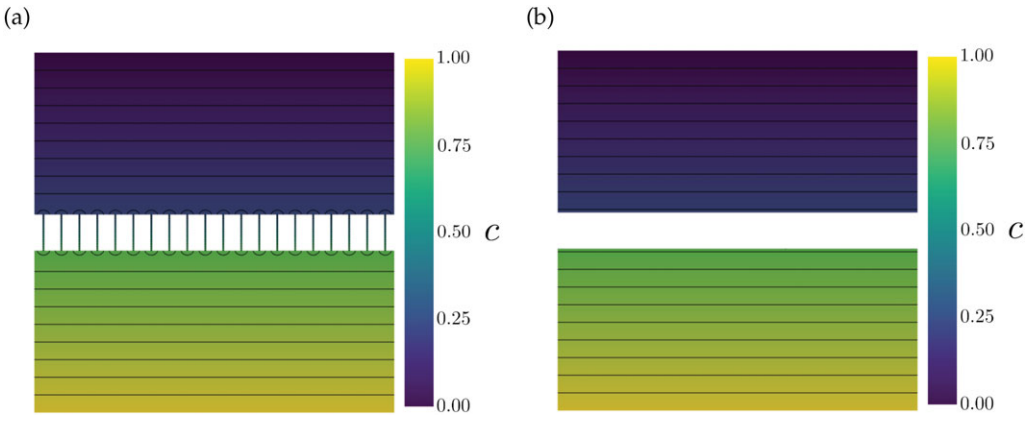

Figure 8. Concentration profile for a membrane with effective permeability $P_{\text{eff}} = 0.189$ and microscale parameters $\delta = 0.25$, $\varepsilon = 0.05$ for (a) a numerical simulation of the full membrane geometry and (b) the analytical solution with our effective interface condition equation (3.35*b*). Contours denote separations of 0.025.

membrane versus time in figure 9b for simulations of the full membrane geometry, simulations using our effective interface conditions, equations (4.12) and (4.13), and simulations using our Euler–Maclaurin early-time approximations for the interface condition, equations (4.14*a*) and (4.14*b*), for two different membrane geometries with effective permeabilities $P_{\text{eff}} = 0.189$ (blue) and $P_{\text{eff}} = 0.953$ (red). We see good agreement between all three simulations in both membranes, noting that we have simulated the Euler–Maclaurin approximations to $t = 2.75$, beyond which they start to deviate more significantly from the other two simulations. We see convergence towards the steady flux value calculated from equations (3.35*b*) and (5.1). We quantify the accuracy of the average flux in fig. S1b in electronic supplementary material, §2.

6. Permeability regimes and implications

The straightforward nature of our derived steady coupling conditions in the long thin channel limit, equations (3.35*a*) and (3.35*b*), means that we can explicitly evaluate the contributions of the microstructure on the resulting macroscale membrane permeability. Our effective permeability coefficient equation (3.35*b*) depends explicitly on the microscale membrane geometry through

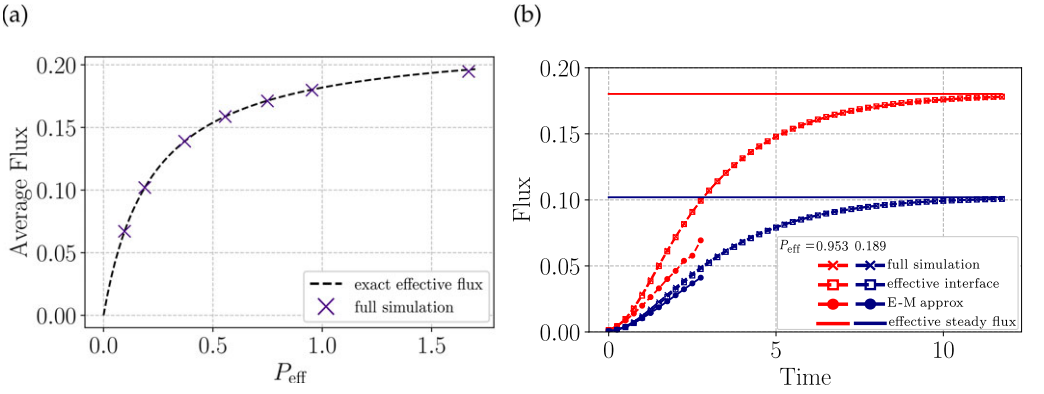

Figure 9. (a) Average flux versus effective permeability in the steady long thin channel problem, equation (3.35*b*). The black dashed line shows the analytical flux calculated from equation (5.1), with the full simulation added as purple crosses. (b) Average flux versus time in the unsteady problem for two different membrane geometries with steady effective permeabilities of 0.189 (blue) and 0.953 (red). We plot the flux for a numerical simulation of the full geometry (crosses), a numerical simulation of the effective interface condition with the infinite sum truncated at 30 terms, equations (4.12) and (4.13), (squares) and a numerical simulation of the Euler–Maclaurin condition, equations (4.14), up to $t = 2.75$ (circles). The solid lines give the steady effective flux of the membrane geometry simulation calculated from equation (5.1). In both plots, flux is calculated over a horizontal line away from the membrane.

the non-dimensional parameters, L, δ and ε, representing the channel length, spacing and the ratio of channel width to spacing, respectively.

We can write our permeability, equation (3.35*b*), as

$$P_{\text{eff}} \sim \frac{1}{\alpha_1 + \alpha_2} \quad \text{with } \alpha_1 = \frac{L}{\varepsilon} \quad \text{and} \quad \alpha_2 = \frac{2\delta}{\pi} \log \frac{1}{8\varepsilon}, \tag{6.1}$$

where α_1 represents channel length effects and α_2 represents the combined effects of the channel opening and interactions between neighbouring channels. With this notation, we can straightforwardly explore the dominant contributions of each physical effect by the relative sizes of our parameter groupings, as shown in figure 10. In each regime in figure 10, our effective membrane condition will take the form of equation (3.35*a*), but with the effective permeability, equation (3.35*b*), taking a different form depending on the limiting factor inhibiting transport. A higher permeability coefficient means the membrane is offering less resistance to transport, whereas a lower permeability coefficient means more resistance to transport.

Regimes 1 and 2 are shown in green in the lower-right-hand half of figure 10. Here, transport is limited by channel length effects, with $\alpha_1 \gg \alpha_2$, and we can write the effective permeability as $P_{\text{eff}} \sim 1/\alpha_1 = L/\varepsilon$. In these regimes, the effective permeability can be both large (in regime 1 if $L \ll \varepsilon$) and small (in regime 2 if $L \gg \varepsilon$), depending on the relative size of channel length compared to the ratio of channel width to spacing.

Regimes 3 and 4 are shown in purple in the upper-left-hand half of figure 10. Here, the limiting factor in transport is channel opening and pore–pore interaction effects, with $\alpha_2 \gg \alpha_1$, and so we write the effective permeability as $P_{\text{eff}} \sim 1/\alpha_2 = \pi/(-2\delta \log 8\varepsilon)$. Here, we can also have both small and large effective permeabilities, depending on the relative sizes of channel width to channel separation. Specifically, the effective permeability is small in regime 3 (where $8\varepsilon \ll \exp(-\pi/2\delta)$), and it is large in regime 4 (where $8\varepsilon \gg \exp(-\pi/2\delta)$). This difference in system behaviour depends on the size of ε compared to an exponentially small function of $\delta \ll 1$. This critical behaviour when $\varepsilon = \mathcal{O}(\exp(-\pi/2\delta))$ agrees with the 2D critical scalings obtained in [22], in which the authors also rigorously prove the form of the limiting problem for the thick Neumann sieve in n dimensions for $n \geqslant 3$, and [29,30], in which the authors derive several models to describe shielding effects of the Faraday cage, including a homogenized continuum model.

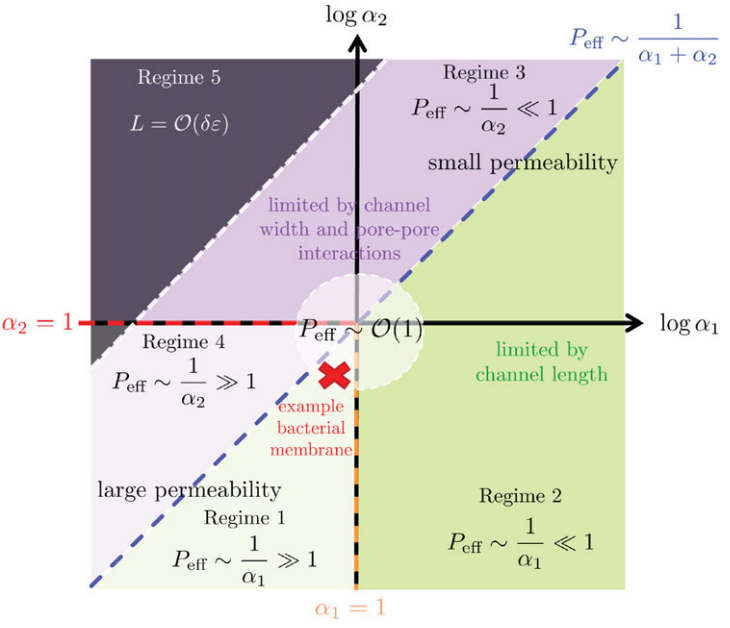

Figure 10. Schematic showing how different parameter regimes of our microscale geometry affect the effective membrane permeability, equation (3.35*b*), in the steady long thin channel limit. We group our parameters into $\alpha_1 = L/\varepsilon$ and $\alpha_2 = 2\delta/\pi \log(1/8\varepsilon)$, where L is the non-dimensional channel length, δ is the channel spacing and ε is the ratio of channel width to channel spacing. The white dotted line is given by $\log\alpha_2 = \log\alpha_1 + \log(2/\pi \log 1/8\varepsilon)$ and marks the boundary in parameter space in which we cross into the $\mathcal{O}(1)$ aspect ratio limit. The dotted circle in the centre represents the scalings giving an $\mathcal{O}(1)$ effective permeability. When $L = \mathcal{O}(\delta\varepsilon)$, the white dotted line coalesces with the blue dashed line. Above the blue dashed line (in the purple region), permeability is dominated by channel width and pore–pore interaction effects, and below this line (in the green region), it is dominated by channel length effects. Taking $R^* = 360$ nm, $r^* = 10$ nm, $a^* = 0.325$ nm and $2L^* = 12$ nm, from table 1, we mark an example bacterial membrane by a red cross with $(\log\alpha_1, \log\alpha_2) = (-0.65, -3.73)$.

Regime 5 arises in the top left of figure 10, and is shaded grey. Here our long thin channel analysis technically breaks down as $\delta\varepsilon = O(L)$ and the analysis of our $\mathcal{O}(1)$ aspect ratio limit holds. However, from figure 6, we see that our long thin channel limit still provides a good estimate of the effective permeability as we move into regime 5, therefore we expect transport to be limited by channel opening and pore–pore interaction effects as in regimes 3 and 4.

(a) Applications to bacterial membranes

Using the parameter values in table 1, we find a range of $-7 \lesssim \log\alpha_1 \lesssim -0.6$ and $\log\alpha_2 \lesssim -3.6$, with permeabilities mostly found in regime 1, implying permeability in bacterial membranes is likely to be largely dominated by channel length effects. Taking our example parameters from before of $R^* = 360$ nm, $r^* = 10$ nm, $a^* = 0.325$ nm and $2L^* = 12$ nm, we obtain $\log\alpha_1 = -0.65$ and $\log\alpha_2 = -3.73$ placing us in a regime where permeability is $\mathcal{O}(1)$ and dominated by channel length effects, with $P_{\text{eff}} \approx 1.9$. We mark this by a red cross on figure 10, noting that these parameters are from a range of Gram-negative bacteria, and the membrane geometry of specific bacteria could lead to larger or smaller permeabilities with a potentially different limiting factor, which can be calculated using equation (3.35*b*).

We predict that transport is limited by channel length effects when $\log\alpha_2 > \log\alpha_1$. In dimensional parameters (defined in equation (2.2)), this is equivalent to $L^* < 2a^*/\pi \log(r^*/8a^*)$. Using this, we can predict how changes to the membrane microstructure could alter the limiting effect on transport. It is known that bacterial cells downregulate expression of porin genes in

response to environmental stresses, allowing them to, for example, reduce intracellular antibiotic concentrations [28]. This effectively increases r^* which could push permeability into channel width and entrance limited regimes. Similarly, mutant strains that show higher resistance to antibiotics are also found to express porins with reduced diameters, decreasing permeability by reducing a^* which can also shift behaviour into channel width and entrance limited regimes [8].

To complete our interpretation, we return to the full steady permeability equation, converting equations (3.35) to dimensional variables using the transformations equation (2.2) and the parameter relations equation (2.5), obtaining

$$D^* \frac{\partial c^*}{\partial y^*}|_{y^*=L^*} = D^* \frac{\partial c^*}{\partial y^*}|_{y^*=-L^*} = \frac{a^* D^*}{r^*(L^* + (2a^*/\pi)[\log(r^*/8a^*) + 1])}[c^*]^{L^*}_{-L^*}, \tag{6.2}$$

where we have multiplied through by the diffusivity D^* to turn the first two terms into genuine diffusive fluxes. We can write the effective coupling conditions equation (6.2) independently of D^* owing to their steady nature, but the unsteady conditions have a genuine D^* dependence. The dimensional formulation equation (6.2) allows us to directly consider the implications of the physical microscale geometry. Writing our channel length as $l^* = 2L^*$ and our channel width as $w^* = 2a^*$, our dimensional permeability coefficient is given by

$$P^*_{\text{eff}} = \frac{w^*}{r^*(l^* + (2w^*/\pi)[\log(r^*/4w^*) + 1])}. \tag{6.3}$$

It is instructive to compare our derived effective permeability equation (6.3) to the constitutive permeability one might pose assuming there are no interactions between porins. That is, to compare equation (6.3) to the density of porins multiplied by the flux J through a single isolated porin, calculated in [8] to be

$$J = \frac{A^* D^*}{l^*} \Delta c^*. \tag{6.4}$$

In equation (6.4), A^* represents the cross-sectional area of the porin (cf w^* here), l^* represents the length of the porin, D^* is the diffusivity of c^*, and Δc^* represents the difference in concentration at either end of the porin. If each porin has an independent effect on the flux, the total effect of all the porins on the macroscale membrane flux is

$$\text{density} \times J = \frac{1}{r^*} \times \frac{A^* D^*}{l^*} \Delta c^*. \tag{6.5}$$

Our result equation (6.3) takes the same form as equation (6.5) in the limit in which permeability is dominated by porin length effects. That is, in regimes 1 and 2 (figure 10) where $L/\varepsilon \gg (-2\delta/\pi)\log 8\varepsilon$, equation (6.2) reduces to

$$D^* \frac{\partial c^*}{\partial y^*} \approx \frac{1}{r^*} \frac{w^* D^*}{l^*}[c^*]^{L^*}_{-L^*}, \tag{6.6}$$

where the right-hand sides of both equations (6.6) and (6.5) follow the same structure:

$$\text{density} \times \frac{\text{channel cross-sectional 'area'} \times \text{diffusivity}}{\text{channel length}} \times \text{concentration difference}. \tag{6.7}$$

We can understand this limit of our permeability equation to represent the case where there are no interactions between porins and each contributes individually to the overall flux. We can therefore interpret $2w^*/\pi[\log r^*/4w^* + 1]$, the term remaining in equation (6.3), as encoding the effect of the interaction between porins on membrane permeability.

(b) Analogy to resistivity

Since the permeability P^*_{eff} is the reciprocal of the effective resistance imposed by the membrane, R^*_{tot}, we can use our explicit result equation (6.3) to assess the individual contributions of microscale geometry to the effective resistance. This allows us to draw analogies with the

resistance offered by resistors in an electrical circuit. Specifically, using the relation $P^*_{\text{eff}} = 1/R^*_{\text{tot}}$ and equation (6.3), we can write

$$\frac{R^*_{\text{tot}}}{r^*} = \frac{l^*}{w^*} + \frac{2}{\pi} + \frac{2}{\pi}\log\frac{1}{4w^*}, \tag{6.8}$$

where the left-hand side represents the effective resistance multiplied by the porin density $1/r^*$. Equation (6.8) is analogous to the total resistance of an electrical circuit, given in terms of the resistance of resistors in series. With this analogy, we consider the contributions to total resistance that the concentration transport has to overcome in order to cross the membrane. The first term on the right-hand side of equation (6.8) relates to the resistance of the channel length, the second to a constant resistance (purely affected by the density of porins) and the third to the resistance offered by the porin openings. The interplay between how these various aspects of the microscale geometry affect permeability (and membrane resistance) is encoded in equations (6.3) and (6.8). Specifically we see that, as one might expect physically, thicker membranes (larger l^*), narrower channels (smaller w^*) and larger channel spacing (larger r^*) all lead to increased resistance and therefore decreased membrane permeability. Our results quantify the relative importance of these effects explicitly in terms of the membrane geometry.

7. Discussion

In this paper, we systematically derived effective coupling conditions for concentrations of solutes diffusing through narrow gaps in an otherwise impermeable membrane, allowing us to couple the concentration on either side of the membrane. We explored the limit in which membrane thickness is much greater than gap width, which we called the long thin channel limit, and the limit in which membrane thickness is of similar size to gap width, which we referred to as the $\mathcal{O}(1)$ aspect ratio limit. In the steady problem, the effective coupling conditions for both limits took the form of an effective permeability condition, equation (1.1), written in terms of the concentration difference across the membrane and an effective permeability coefficient given by equations (3.35*b*) and (3.40) in the long thin channel and $\mathcal{O}(1)$ aspect ratio limits, respectively. This coefficient depends explicitly on the microscale geometry of the membrane, through the non-dimensional parameters, L, δ and ε, representing the gap length, spacing and the ratio of gap width to spacing, respectively. Using this effective permeability coefficient, we were able to explore how changes in membrane microstructure alter the resulting permeability of the membrane, and explore various sublimits of the problem to determine the limiting factors affecting transport, and resulting size of the effective permeability. These results are summarized schematically in figure 10.

When considering the full time-dependent problem, the added complexity of the time it takes the solute to diffuse across the channel is captured within the infinite sums in our coupling conditions equations (4.12) and (4.13). We see that the coupling conditions gain a memory property encoded through the time integrals in equations (4.12) and (4.13). Provided that the outer concentration tends to a steady solution in the long time limit, i.e. $\dot{c}_{\pm} \to 0$, we find that the memory contribution decays and we recover the steady coupling conditions. Care needs to be taken evaluating the integrals and infinite sums in the limit $t \to 0^+$, where the sums are slow to converge. Here, we approximate the infinite sums using an Euler–Maclaurin approximation to obtain simpler effective coupling conditions, as given in equations (4.14) and derived in electronic supplementary material, §1. This early-time approximation gives us insight into how the time-dependent conditions scale with t and allow for faster simulations at early times, removing the need to include many terms in the infinite sums of equations (4.12) and (4.13). For both the steady and time-dependent problems, we validated the derived effective coupling conditions against simulations of the full membrane structure, as shown in §5. We anticipate that our results could be used to generate reduced continuum models to describe diffusion problems in complex geometries such as examples explored in [49], where the authors propose new numerical methods for these problems, exploiting Laplace transforms and boundary integral methods.

In this paper, our primary application of interest was the outer membrane of Gram-negative bacteria. Using our steady effective conditions, equations (3.35), we explored how the microstructure of this membrane affects its resulting permeability in §6. With typical parameter values from a range of Gram-negative bacteria, as listed in table 1, we find that permeability is likely to be dominated by the membrane thickness, i.e. channel length, but hypothesize that reduced porin expression could lead to channel entrance effects becoming the limiting factor as porins become sparse. Both of these behaviours are captured in equation (3.35*b*), from which we can obtain the appropriate form for the effective permeability in each limit, as discussed in §6, and which can be used to calculate permeabilities specific to individual bacterial species. We also provide an explicit form for the effective permeability in the limit of $\mathcal{O}(1)$ aspect ratio channels in equation (3.40), for example representing thinner membranes or wider porins, and calculate the appropriate effective conditions to use when the concentrations inside or outside the cell are time-varying in equations (4.12) and (4.13).

It would be interesting to consider different membrane geometries and asymptotic limits in the future. For example, in [36], the authors found that porins form clustered patches in the outer membrane of *E. coli*, suggesting a membrane geometry with periodic patches of porin-free and porin-dense regions is biologically relevant. This could also potentially be explored by adapting the techniques of [50], where the author considered periodic windows of slots in a superhydrophobic grooved surface. More generally, the limit in which the width of our impermeable chunks goes to zero ($r^* - 2a^* \to 0$) could be of mathematical interest, as it may allow for fully analytical solutions of the problem, by extending the conformal mapping techniques used in [50–52] to the domains here.

In this paper, we considered membrane transport in 2D for simplicity. Through this, we have identified key parameter groupings which determine the limiting factor for membrane transport. An analysis of three-dimensional (3D) membrane transport would be an interesting extension to this work. We anticipate that while similar types of parameter groupings may determine the qualitative behaviour of membrane transport in 3D, the shape of the porin entrance and 3D geometry play important roles. We therefore expect different functional forms of the membrane permeability in terms of membrane geometry; notably, the logarithmic singularity in equations (3.35*b*) and (3.40) is probably a 2D phenomenon. More generally, one would not be able to rely on complex conformal maps to solve our inner regions in 3D.

Our physical parameter values, listed in table 1, imply that cell radius is much larger than the membrane thickness, meaning curvature is small for spherical bacteria. Although we have neglected membrane curvature altogether in our model, we expect our derived coupling conditions, equations (3.35), (3.40), (4.12) and (4.13), to hold for membranes with non-zero curvature, provided the curvature is not too large as to be observable in our boundary layer and inner regions. Similar leading-order independence of curvature is seen in [53], when looking at asymptotic solutions of mean first passage time problems in non-spherical 3D domains, and in [54], where the authors consider concentration differences between narrow windows on curved surfaces generated by localized diffusive fluxes. We note that, for a weakly curved membrane, it should be possible to systematically obtain higher-order corrections to our coupling conditions which explicitly depend on curvature, for example by using curvilinear coordinates in our boundary layer problems in §3b, representing a small perturbation to flat space, e.g. [55].

Furthermore, although we present our model in the context of a concentration, c, the problem set-up can be reframed in terms of probability density functions describing particle position, with only minor modifications to the subsequent analysis. In particular, one can consider equation (2.1*a*) as a drift-free Fokker–Planck equation for the position of the centre of a finite-sized particle, and reframe a modified membrane geometry as the effective space in which the particle can move. As a result, we anticipate that these results could be adapted in future work to describe transport of finite-sized particles, with some differences introduced from particle shape and interactions altering the effective geometry.

The effective coupling conditions that we have derived, equations (3.35) and (3.40), and equations (4.12) and (4.13), for the steady and unsteady problems, respectively, could be applied

to the even larger scale of bacterial colony dynamics, if combined with upscaling methods such as [56,57], to obtain a fully multiscale model that systematically accounts for membrane-level effects. In this paper, we focused on membrane geometry parameters relevant to bacterial membranes; however transport across membrane-type structures is important in many other contexts, including nutrient transport, waste removal, mass transfer through surface coatings in chemical engineering, water vapour loss through fabrics and carbon dioxide absorption on plant leaves via stomata [13,58–60]. The results in this work therefore have a much wider reach of applications, and may be used to understand diffusive transport through periodic narrow gaps in many contexts.

Data accessibility. The computational tools are freely available at https://github.com/MollyB06/2d-effective-perm-paper.

The data are provided in the electronic supplementary material [61].

Declaration of AI use. We have not used AI-assisted technologies in creating this article.

Authors' contributions. M.B.: formal analysis, investigation, methodology, writing—original draft, writing—review and editing; E.F.Y.: methodology, supervision, writing—review and editing; P.P.: conceptualization, supervision, writing—review and editing; M.P.D.: conceptualization, methodology, supervision, writing—review and editing. All authors gave final approval for publication and agreed to be held accountable for the work performed therein.

Conflict of interest declaration. We declare we have no competing interests.

Funding. E.F.Y. is supported by an EPSRC National Fellowship in Fluid Dynamics (grant no. EP/X027902/1), P.P. is supported by a UKRI Future Leaders Fellowship (grant no. MR/V022385/1). For the purpose of open access, the authors have applied a Creative Commons Attribution (CC BY) licence to any Author Accepted Manuscript version arising from this submission.

Appendix A. $\mathcal{O}(1)$ aspect ratio derivation

In this appendix, we derive the $\mathcal{O}(1)$ aspect ratio effective permeability, equation (3.40). As discussed in §3d, the main change from the long thin channel limit is the coalescence of the three inner regions IIIa–c into a single inner region. As in §3a, we start by scaling into this inner region using the transformations

$$x = \delta\varepsilon X \quad \text{and} \quad y = \delta\varepsilon Y, \tag{A 1}$$

which converts equations (2.3) into the scaled system

$$\frac{\partial^2 c}{\partial X^2} + \frac{\partial^2 c}{\partial Y^2} = 0 \quad \text{for } \{X \in \mathbb{R}, |Y| > a\} \cup \{|X| < 1, |Y| < a\} \tag{A 2a}$$

and

$$\frac{\partial c}{\partial n} = 0 \quad \text{for } \{|X| > 1, |Y| = a\} \cup \{|X| = 1, |Y| < a\}. \tag{A 2b}$$

We again only require the leading-order problem and work directly with equation (A 2), using a conformal map to simplify our domain. Setting $Z = X + iY$, we follow a similar procedure to §3a(ii), but for a different mapping. The map between the physical domain and the upper-half-plane is shown in figure 11, which we can then straightforwardly map to the semi-infinite strip in which we solve our problem. The Schwarz–Christoffel map from the upper-half-plane to the physical domain is

$$Z = X + iY = f(\omega) = \tilde{P} + \tilde{d}\int_a^{\omega} \frac{(u^2-1)^{1/2}(u^2-\lambda^2)^{1/2}}{u^2}\,\mathrm{d}u. \tag{A 3}$$

The constant λ is defined as the preimage of the point $1 + ai$ in the Z domain and is determined implicitly. We can rewrite equation (A 3) in a more interpretable form using the change of

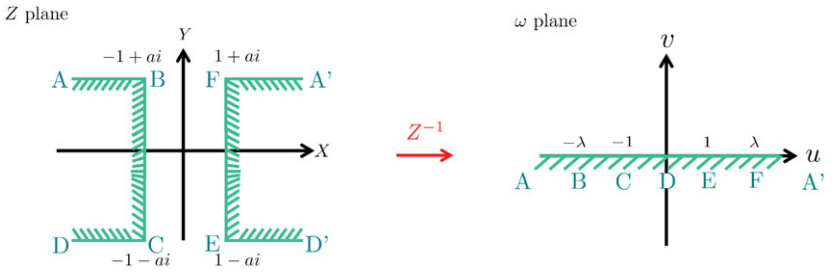

Figure 11. Schematic showing the result of the inverse of the conformal map equation (3.36), transforming our physical gap domain in Z to the upper-half-plane in ω. The variable λ describing the preimage of the point $1 + ai$ under the map Z is determined by the geometry and given implicitly in equation (3.39).

variables $t = 1/u$, integrating by parts and redefining the constant terms to obtain

$$Z = P + d\left\{\omega\left(1 - \frac{1}{\omega^2}\right)^{1/2}\left(1 - \frac{\lambda^2}{\omega^2}\right)^{1/2} + \int_0^{1/\omega} \frac{(1-\lambda^2 t^2)^{1/2}}{(1-t^2)^{1/2}}\mathrm{d}t + \lambda\int_0^{\lambda/\omega} \frac{(1-(1/\lambda^2)t^2)^{1/2}}{(1-t^2)^{1/2}}\mathrm{d}t\right\}, \tag{A 4}$$

where P, d are the new constants. Our integral terms in equation (A 4) are now in the form of incomplete elliptic integrals of the second kind. We must take care when choosing our branch cuts across all of the square-root terms in equation (A 4). In particular, because ω lies in the upper half-plane, $1/\omega$ is in the lower half-plane. Hence, we choose our branch cuts to extend into the upper-half-plane from the points $-1, -1/\lambda, 1/\lambda, 1$ on the real axis, thus avoiding intersections with the physical domain. Using the desired geometry of our physical domain in Z and the symmetry of the problem, we set our unknown constants P and d to arrive at equation (3.36) as given in §3d, with d defined in equation (3.38). The dependence of λ on a is implicitly given through the relation equation (3.39).

As in §3a(ii), we further map into the semi-infinite strip to solve our problem and then transform back into the upper-half-plane to write our solution implicitly in terms of ω, obtaining

$$c \sim \frac{2b}{\pi}\log|\omega| + e. \tag{A 5}$$

Since equation (3.36) is not explicitly invertible, we use its limiting form as $|\omega| \to 0, \infty$ to match into our boundary layer regions by writing equation (A 5) in terms of X and Y. To match with region IV, the boundary layer below the membrane, we take the limit $|\omega| \to 0$. In this limit, equations (3.36) and (A 5) take the form

$$Z \sim -\frac{d\lambda}{\omega}, \quad c \sim \frac{2b}{\pi}\log|d\lambda| - \frac{2b}{\pi}\log|Z| + e \quad \text{as } |\omega| \to 0. \tag{A 6}$$

Similarly to match into region II, the boundary layer above the membrane, we take the limit as $|\omega| \to \infty$, obtaining the limiting forms of equations (3.36) and (A 5):

$$Z \sim -\mathrm{d}\omega, \quad c \sim \frac{2b}{\pi}\log|Z| - \frac{2b}{\pi}\log|d| + e \quad \text{as } |\omega| \to \infty. \tag{A 7}$$

Finally, we also match equations (A 6) and (A 7) to our boundary layer solutions, equations (3.26) and (3.28), in the limits $Y_{1,2} \to 0_{-,+}$ to obtain

$$\kappa_1 = -\kappa_2 \quad \text{and} \quad A_1 = A_2 + \frac{\kappa_2}{\pi}\log\varepsilon^2\pi^2\lambda d^2. \tag{A 8}$$

Using equations (3.32), the previous matching between the boundary layer regions and the outer regions, to give $\kappa_{1,2}$ and $A_{1,2}$ in terms of the outer concentrations and fluxes, we obtain our $\mathcal{O}(1)$ aspect ratio coupling conditions with permeability equation (3.40).

References

1. Haney P, Herting K, Smith S. 2013 Separation characteristics of dialysis membranes. In *Pierce previews. Pierce protein biology products*, pp. 2–6.
2. Cancilla N, Gurreri L, Ciofalo M, Cipollina A, Tamburini A, Micale G. 2025 Mathematical modelling of hollow-fiber haemodialysis modules. *Phys. Sci. Rev.* **10**, 11–50. (doi:10.1515/psr-2024-0062)
3. Aninwede C, Kratky L. 2025 Modeling trends in multicomponent gas membrane separation process: a review. *J. Eng. Appl. Sci.* **72**, 1–19. (doi:10.1186/s44147-025-00608-w)
4. Dżygiel P, Wieczorek PP. 2010 *Supported liquid membranes and their modifications: definition, classification, theory, stability, application and perspectives*, pp. 73–140. Amsterdam, Netherlands: Elsevier.
5. Tieleman DP. 2005 Computer simulations of transport through membranes: passive diffusion, pores, channels and transporters. In *Proc. Aust. Physiol. Soc., Canberra, September 2005*, vol. 37, pp. 15–27.
6. Linares OA, Schiesser WE, Fudin J, Pham TC, Bettinger JJ, Mathew RO, Daly AL. 2015 In silico ordinary differential equation/partial differential equation hemodialysis model estimates methadone removal during dialysis. *J. Pain Res.* **8**, 417–429. (doi:10.2147/JPR.S84615)
7. Melke P, Sahlin P, Levchenko A, Jönsson H. 2010 A cell-based model for quorum sensing in heterogeneous bacterial colonies. *PLoS Comput. Biol.* **6**, e1000819. (doi:10.1371/journal.pcbi.1000819)
8. Prajapati JD, Kleinekathöfer U, Winterhalter M. 2021 How to enter a bacterium: bacterial porins and the permeation of antibiotics. *Chem. Rev.* **121**, 5158–5192. (doi:10.1021/acs.chemrev.0c01213)
9. Schiesser WE. 2013 *Partial differential equation analysis in biomedical engineering: case studies with MATLAB*. Cambridge, England: Cambridge University Press.
10. Wong E. 2009 *Cells: molecules and mechanisms*. Louisville, Kentucky, USA: Axolotl Academic Publishing.
11. Barbarossa MV, Kuttler C. 2016 Mathematical modeling of bacteria communication in continuous cultures. *Appl. Sci.* **6**, 149. (doi:10.3390/app6050149)
12. Goryachev A, Toh D, Lee T. 2006 Systems analysis of a quorum sensing network: design constraints imposed by the functional requirements, network topology and kinetic constants. *Biosystems* **83**, 178–187. (doi:10.1016/j.biosystems.2005.04.006)
13. Wakeham WA, Mason EA. 1979 Diffusion through multiperforate laminae. *Ind. Eng. Chem. Fundam.* **18**, 301–305. (doi:10.1021/i160072a001)
14. Belyaev AG, Chechkin GA, Gadyl'shin RR. 1999 Effective membrane permeability: estimates and low concentration asymptotics. *SIAM J. Appl. Math.* **60**, 84–108. (doi:10.1137/S0036139996312880)
15. Bernoff AJ, Lindsay AE, Schmidt DD. 2018 Boundary homogenization and capture time distributions of semipermeable membranes with periodic patterns of reactive sites. *Multiscale Model. Simul.* **16**, 1411–1447. (doi:10.1137/17M1162512)
16. Bruna M, Chapman S, Ramon G. 2015 The effective flux through a thin-film composite membrane. *Europhys. Lett.* **110**, 40005. (doi:10.1209/0295-5075/110/40005)
17. Lindsay AE, Bernoff AJ, Ward MJ. 2017 First passage statistics for the capture of a Brownian particle by a structured spherical target with multiple surface traps. *Multiscale Model. Simul.* **15**, 74–109. (doi:10.1137/16M1077659)
18. Muratov CB, Shvartsman SY. 2008 Boundary homogenization for periodic arrays of absorbers. *Multiscale Model. Simul.* **7**, 44–61. (doi:10.1137/070692832)
19. Zampogna GA, Gallaire F. 2020 Effective stress jump across membranes. *J. Fluid Mech.* **892**, A9. (doi:10.1017/jfm.2020.144)
20. Zampogna GA, Ledda PG, Gallaire F. 2022 Transport across thin membranes: effective solute flux jump. *Phys. Fluids* **34**, 083113. (doi:10.1063/5.0101621)
21. Bhattacharya A, Gahn M, Neuss-Radu M. 2022 Effective transmission conditions for reaction–diffusion processes in domains separated by thin channels. *Appl. Anal.* **101**, 1896–1910. (doi:10.1080/00036811.2020.1789599)
22. Del Vecchio T. 1987 The thick Neumann's sieve. *Annu. Math. Pura Appl.* **147**, 363–402. (doi:10.1007/BF01762424)
23. Marušić S. 2008 An asymptotic expansion for the Neumann sieve problem. *Russ. J. Math. Phys.* **15**, 89–97. (doi:10.1134/S106192080801010X)

24. Raveendran V, Cirillo E, Muntean A. 2022 Upscaling of a reaction–diffusion–convection problem with exploding non-linear drift. *Q. Appl. Math.* **80**, 641–667. (doi:10.1090/qam/1622)
25. Dalwadi MP, Pearce P. 2021 Emergent robustness of bacterial quorum sensing in fluid flow. *Proc. Natl Acad. Sci. USA* **118**, e2022312118. (doi:10.1073/pnas.2022312118)
26. Miller MB, Bassler BL. 2001 Quorum sensing in bacteria. *Annu. Rev. Microbiol.* **55**, 165–199. (doi:10.1146/annurev.micro.55.1.165)
27. Naga NG, El-Badan DE, Ghanem KM, Shaaban MI. 2023 It is the time for quorum sensing inhibition as alternative strategy of antimicrobial therapy. *Cell Commun. Signal.* **21**, 1–14. (doi:10.1186/s12964-023-01154-9)
28. Vergalli J *et al.* 2020 Porins and small-molecule translocation across the outer membrane of Gram-negative bacteria. *Nat. Rev. Microbiol.* **18**, 164–176. (doi:10.1038/s41579-019-0294-2)
29. Chapman SJ, Hewett DP, Trefethen LN. 2015 Mathematics of the faraday cage. *SIAM Rev.* **57**, 398–417. (doi:10.1137/140984452)
30. Hewett DP, Hewitt IJ. 2016 Homogenized boundary conditions and resonance effects in faraday cages. *Proc. R. Soc. A* **472**, 20160062. (doi:10.1098/rspa.2016.0062)
31. Delourme B, Haddar H, Joly P. 2012 Approximate models for wave propagation across thin periodic interfaces. *J. Math. Pures Appl.* **98**, 28–71. (doi:10.1016/j.matpur.2012.01.003)
32. Delourme B, Haddar H, Joly P. 2013 On the well-posedness, stability and accuracy of an asymptotic model for thin periodic interfaces in electromagnetic scattering problems. *Math. Models Methods Appl. Sci.* **23**, 2433–2464. (doi:10.1142/S021820251350036X)
33. Marigo JJ, Maurel A. 2016 Homogenization models for thin rigid structured surfaces and films. *J. Acoust. Soc. Am.* **140**, 260–273. (doi:10.1121/1.4954756)
34. Bakshi S, Siryaporn A, Goulian M, Weisshaar JC. 2012 Superresolution imaging of ribosomes and RNA polymerase in live *Escherichia coli* cells. *Mol. Microbiol.* **85**, 21–38. (doi:10.1111/j.1365-2958.2012.08081.x)
35. Hau HH, Gralnick JA. 2007 Ecology and biotechnology of the genus *Shewanella*. *Annu. Rev. Microbiol.* **61**, 237–258. (doi:10.1146/annurev.micro.61.080706.093257)
36. Benn G *et al.* 2021 Phase separation in the outer membrane of *Escherichia coli*. *Proc. Natl Acad. Sci. USA* **118**, e2112237118. (doi:10.1073/pnas.2112237118)
37. Bayer M. 1991 Zones of membrane adhesion in the cryofixed envelope of *Escherichia coli*. *J. Struct. Biol.* **107**, 268–280. (doi:10.1016/1047-8477(91)90052-X)
38. Mai-Prochnow A, Clauson M, Hong J, Murphy AB. 2016 Gram positive and Gram negative bacteria differ in their sensitivity to cold plasma. *Sci. Rep.* **6**, 38610. (doi:10.1038/srep38610)
39. Niederweis M. 2003 Mycobacterial porins—new channel proteins in unique outer membranes. *Mol. Microbiol.* **49**, 1167–1177. (doi:10.1046/j.1365-2958.2003.03662.x)
40. Amako K, Wai SN, Umeda A, Shigematsu M, Takade A. 1996 Electron microscopy of the major outer membrane protein of *Campylobacter jejuni*. *Microbiol. Immunol.* **40**, 749–754. (doi:10.1111/j.1348-0421.1996.tb01136.x)
41. Delcour AH. 2009 Outer membrane permeability and antibiotic resistance. *Biochim. Biophys. Acta Proteins Proteom.* **1794**, 808–816. (doi:10.1016/j.bbapap.2008.11.005)
42. Carrier GF, Krook M, Pearson CE. 2005 *Functions of a complex variable: theory and technique*. Philadelphia, Pennsylvania, USA: SIAM.
43. Constantin E, Pavel N. 2010 Green function of the Laplacian for the Neumann problem in $\mathbb{R}^n_+$. *Lib. Math.* **30**, 57–70.
44. Alnaes MS, Logg A, Ølgaard KB, Rognes ME, Wells GN. 2014 Unified form language: a domain-specific language for weak formulations of partial differential equations. *ACM Trans. Math. Softw.* **40**, 1–37. (doi:10.1145/2566630)
45. Barrata IA *et al.* 2023 DOLFINx: the next generation FEniCS problem solving environment.
46. Scroggs MW, Baratta IA, Richardson CN, Wells GN. 2022 Basix: a runtime finite element basis evaluation library. *J. Open Source Softw.* **7**, 3982. (doi:10.21105/joss.03982)
47. Scroggs MW, Dokken JS, Richardson CN, Wells GN. 2022 Construction of arbitrary order finite element degree-of-freedom maps on polygonal and polyhedral cell meshes. *ACM Trans. Math. Softw.* **48**, 1–23. (doi:10.1145/3524456)
48. Geuzaine C, Remacle J-F. 2009 Gmsh: a 3-D finite element mesh generator with built-in pre-and post-processing facilities. *Int. J. Numer. Methods Eng.* **79**, 1309–1331. (doi:10.1002/nme.2579)
49. Cherry J, Lindsay AE, Quaife BD. 2025 Boundary integral methods for particle diffusion in complex geometries: shielding, confinement, and escape. *J. Comput. Phys.* **534**, 114032. (doi:10.1016/j.jcp.2025.114032)

50. Crowdy DG. 2021 Slip length formulas for longitudinal shear flow over a superhydrophobic grating with partially filled cavities. *J. Fluid Mech.* **925**, R2. (doi:10.1017/jfm.2021.709)
51. Miyoshi H, Rodriguez-Broadbent H, Curran A, Crowdy D. 2022 Longitudinal flow in superhydrophobic channels with partially invaded grooves. *J. Eng. Math.* **137**, 3. (doi:10.1007/s10665-022-10240-9)
52. Miyoshi H, Kirk TL, Hodes M, Crowdy DG. 2024 Fully developed flow through shrouded-fin arrays: exact and asymptotic solutions. *J. Fluid Mech.* **991**, A2. (doi:10.1017/jfm.2024.505)
53. Gomez D, Cheviakov AF. 2015 Asymptotic analysis of narrow escape problems in nonspherical three-dimensional domains. *Phys. Rev. E* **91**, 012137. (doi:10.1103/PhysRevE.91.012137)
54. Paquin-Lefebvre F, Holcman D. 2021 Modelling and asymptotic analysis of the concentration difference in a nanoregion between an influx and outflux diffusion across narrow windows. *Proc. R. Soc. A* **477**, 20210501. (doi:10.1098/rspa.2021.0501)
55. Sbragaglia M, Prosperetti A. 2007 A note on the effective slip properties for microchannel flows with ultrahydrophobic surfaces. *Phys. Fluids* **19**, 043603. (doi:10.1063/1.2716438)
56. Dalwadi MP, King JR. 2020 A systematic upscaling of nonlinear chemical uptake within a biofilm. *SIAM J. Appl. Math.* **80**, 1723–1750. (doi:10.1137/19M130220X)
57. Dalwadi MP, Wang Y, King JR, Minton NP. 2018 Upscaling diffusion through first-order volumetric sinks: a homogenization of bacterial nutrient uptake. *SIAM J. Appl. Math.* **78**, 1300–1329. (doi:10.1137/17M1138625)
58. Baker RW, Low BT. 2014 Gas separation membrane materials: a perspective. *Macromolecules* **47**, 6999–7013. (doi:10.1021/ma501488s)
59. Pappenheimer JR. 1953 Passage of molecules through capillary walls. *Physiol. Rev.* **33**, 387–423. (doi:10.1152/physrev.1953.33.3.387)
60. Stillwell W. 2013 Membrane transport. In *An introduction to biological membranes: from bilayers to rafts*, p. 305.
61. Brennan M, Yeo EF, Pearce P, Dalwadi MP. 2025 Effective permeability conditions for diffusive transport through impermeable membranes with gaps. Figshare. (doi:10.6084/m9.figshare.c.8217042)